



Title	Diurnal precipitation and high cloud frequency variability over the Gulf Stream and over the Kuroshio
Author(s)	Minobe, Shoshiro; Takebayashi, Shogo
Citation	Climate dynamics, 44(7-8), 2079-2095 <a href="https://doi.org/10.1007/s00382-014-2245-y">https://doi.org/10.1007/s00382-014-2245-y</a>
Issue Date	2015-04-01
Doc URL	<a href="http://hdl.handle.net/2115/61072">http://hdl.handle.net/2115/61072</a>
Rights	The final publication is available at <a href="http://link.springer.com">link.springer.com</a>
Type	article (author version)
File Information	ClimDyn_44_p2079-.pdf



[Instructions for use](#)

# Diurnal precipitation and high cloud frequency variability over the Gulf Stream and over the Kuroshio

Shoshiro Minobe and Shogo Takebayashi

*Department of Natural History Sciences, Graduate School of Science, Hokkaido University, Sapporo, Japan*

Submitted to Climate Dynamics, December 10, 2013

Revised, May 20, 2014.

Accepted July 3, 2014.

Corresponding author:

Shoshiro Minobe

Phone/fax: +81-11-706-2644

Mail address: Room 319, Rigaku building No 8, Hokkaido University, N10, W8, Kita-ku, Sapporo 060-0810, Japan

## 1 Abstract

2           Recent studies show mid-latitude western boundary currents (WBCs) substantially influence the  
3 atmosphere aloft, and an important feature is enhanced rain band over the WBCs in climatological mean  
4 field. However, how such long-term, climate phenomena are related to shorter, weather timescale  
5 phenomena are generally remained to be explored. In this paper, diurnal precipitation and cloud variations  
6 are investigated global mid-latitude oceans with emphasis on air-sea interactions over WBCs using  
7 satellite-derived precipitation and outgoing longwave radiation (OLR) datasets.

8           Strong 24-hour period components of precipitations are found over the Gulf Stream in summer  
9 and over the Kuroshio in the East China Sea in early summer (Baiu-Meiyu season), respectively. Similar  
10 diurnal precipitations are not observed in WBCs in the Southern Hemisphere year around. The diurnal  
11 precipitation cycles over the Gulf Stream and the Kuroshio exhibit peak phases in the early to late morning  
12 for the Gulf Stream and late morning to early afternoon for the Kuroshio, with southeastward phase  
13 propagations. High cloud frequency derived from OLR data exhibit consistent diurnal cycles. A substantial  
14 difference of diurnal cycles between the Gulf Stream and the Kuroshio regions are associated with the  
15 large-scale Baiu-Meiyu rain and cloud bands for the latter region. Diurnal precipitation and high cloud  
16 variability is found in the vicinity of the Kuroshio itself, embedded in the Baiu-Meiyu rain and cloud bands  
17 distributing in a wider area without a strong diurnal component. The spatial and seasonal distributions of  
18 the diurnal variability over these WBCs strongly suggests that the diurnal precipitation and cloud cycles are  
19 essential aspects of *deep heating mode* of atmospheric response recently reported for these WBCs. These  
20 results indicate that these WBCs in the Northern Hemisphere play an important role in modulating  
21 short-term precipitation variations, and on the other hand diurnal variability can be a substantial agent for  
22 the mid-latitude air-sea interaction.

23

24

## 25 1. Introduction

26           How mid-latitude oceans fronts, associated with western boundary currents (WBCs) and  
27 meso-scale eddies, influence the overlying atmosphere is a rapidly developing research field. In particular,  
28 air-sea interactions over four mid-latitude WBCs, i.e., the Gulf Stream, the Kuroshio and its extension, the  
29 Agulhas Return Current, and the Brazil-Malvinas currents, have attracted much attention (see reviews by  
30 Chelton et al. 2004; Xie 2004; Small et al. 2008; Chelton and Xie 2010). Among these four regions,  
31 prominent tropospheric responses to the WBCs above the Marine Atmospheric Boundary Layer (MABL)  
32 were reported for the Gulf Stream (Minobe et al. 2008; 2010; Czaja and Blunt 2011), the Kuroshio  
33 Extension (Tokinaga et al. 2009; Czaja and Blunt 2011) and the Kuroshio in the East China Sea (Xu et al.  
34 2011; Sasaki et al. 2012), characterized by enhanced rain accompanied by ascent. Also, cloud distribution  
35 and tropospheric temperatures are modified over the Agulhas Return Current region (Liu et al. 2007;  
36 Shimada and Minobe 2011). These studies, however, mainly investigated seasonal or annual mean  
37 climatologies. The atmospheric responses found in the time mean fields must involve time varying  
38 phenomena on shorter timescales. This is especially true for precipitation, because its occurrence is highly  
39 intermittent and is closely related to shorter timescale phenomena such as synoptic scale disturbances and

40 diurnal variability.

41 Most of the previous studies that have investigated the relation between shorter timescale  
42 phenomena and air-sea interaction over the mid-latitude WBCs have focused on synoptic scale variations.  
43 Synoptic scale disturbances strongly modify air-sea heat fluxes in WBC regions as found in observations  
44 (e.g., Alexander and Scott 1997; Zolina and Gulev 2003; Shaman et al. 2010; Rudeva and Gulev 2011) and  
45 also in modeling studies (e.g., Nonaka et al. 2009; Taguchi et al. 2009; Brayshaw et al. 2011). The sensible  
46 and latent heat fluxes are important in maintaining the surface baroclinicity (e.g., Hoskins and Valdes 1990;  
47 Nakamura et al. 2004, 2008), which is crucial for developments of extratropical cycles (Hoskins et al.  
48 1985) and thus important in determining the nature of the storm tracks (e.g., Inatsu et al. 2003; Inatsu and  
49 Hoskins 2004; Brayshaw et al. 2008, 2011; Ogawa et al. 2012). In particular, surface storm tracks and high  
50 wind distributions are strongly affected by WBCs (Sampe and Xie 2007; Joyce et al. 2009; Booth et al.  
51 2010), and atmospheric latent heating associated with precipitation plays an important role in cyclone  
52 development over WBC regions (e.g., Kuo et al. 1991; Kuwano-Yoshida et al. 2010; Booth et al. 2012).  
53 Furthermore, an observational study by Nakamura et al. (2012) showed that wintertime extratropical  
54 cyclone tracks are modified by the Kuroshio's large meander south of Japan, which was confirmed in the  
55 numerical experiment by Hayasaki et al. (2013).

56 In contrast to the large body of work on synoptic scale variability, the linkage between air-sea  
57 interaction over the WBCs and diurnal variability is much less well studied. Most studies of diurnal  
58 precipitation cycles focused their attention on diurnal variations over land (e.g., Wallace 1975; Oki and  
59 Musiak 1994) or in the tropics (e.g., Janowiak et al. 1994; Yang and Slingo 2001; Nesbitt and Zipser 2003;  
60 Kikuchi and Wang 2008), probably reflecting data availability in early studies and also the overall tendency  
61 for strong diurnal variations over land and/or the tropics. However, one can see that a relatively strong  
62 diurnal cycle of precipitation occurs over the Gulf Stream in a global analysis (Fig. 2 in Kikuchi and Wang  
63 2008) or in a regional analysis focused on North America (Fig. 6 in Dirmeyer et al. 2012) in summer,  
64 though the possible dependency of this diurnal precipitation to the Gulf Stream was not mentioned in these  
65 papers. Diurnal cloud variations over the Gulf Stream region were also reported a decade ago by Alliss and  
66 Raman (1995), though their analysis was limited to the western portion of the Gulf Stream (west of 71°W)  
67 using 6-hourly data, which is coarsely sampled compared with hourly or 3-hourly sampled data used in  
68 recent studies (e.g., Dai et al. 2007; Kikuchi and Wang 2008).

69 Given the fact that the oceanic diurnal precipitations are generally stronger in the tropics than in  
70 the mid-latitudes, it is worthwhile to note that tropical-like atmospheric responses to mid-latitude WBCs  
71 have been identified in recent studies. Minobe et al. (2010) found a stark difference in the atmospheric  
72 response over the Gulf Stream between the summer and winter seasons. In summer, maximum upward  
73 winds are found in the middle of the troposphere, just above the enhanced precipitation over the Gulf  
74 Stream, accompanied by horizontal convergence in the lower troposphere. Atmospheric heating has its  
75 maximum also in the mid-troposphere, where convective latent heating dominates. The authors referred to  
76 this type of atmospheric response as the *deep heating mode*. In winter, upward winds have their maximum  
77 in the lower troposphere (850–700 hPa), and the corresponding horizontal convergence is mostly limited to  
78 the MABL, though summer time convergence is not confined in this layer. The corresponding atmospheric

79 heating consists of sensible heating (including vertical diffusion of heat in the MABL) and convective  
80 latent heating just above the top of the MABL, resulting in total atmospheric heating that exhibits a  
81 maximum in the lower troposphere. The authors referred to this type of atmospheric response as the  
82 *shallow heating mode*, and showed that a bimodal variation of the atmospheric heating profile exists  
83 between deep and shallow distributions.

84 A deep heating mode as energetic as that over the Gulf Stream is also found in the atmospheric  
85 response over the Kuroshio in the East China Sea in June, i.e., middle of early summer rain season in this  
86 region (Sasaki et al. 2012). This long-lasting precipitation phenomenon prevailing from southeast China to  
87 Japan is called Baiu in Japan and Meiyu in China. The Baiu-Meiyu rainband is caused by basin-scale  
88 interactions between the atmosphere, land and the ocean. Moisture transport by low-level jets along the  
89 western flank of the subtropical high is a key factor in generating the Baiu-Meiyu rainband (e.g., Ninomiya  
90 and Akiyama 1992), whereas horizontal temperature advection from the Tibetan Plateau also plays an  
91 important role in determining its location (Sampe and Xie 2010). Sasaki et al. (2012) found that a localized  
92 atmospheric response to the Kuroshio, with the deep heating mode, is embedded in the large-scale  
93 Baiu-Meiyu rainband. A weak deep heating mode is also observed over the Kuroshio Extension in summer  
94 (Minobe et al. 2010; Tokinaga et al. 2009), and over the East China Sea in spring (Xu et al. 2011). The  
95 presence of tropical-like atmospheric responses to the Gulf Stream may be related to the aforementioned  
96 diurnal precipitation over the Gulf Stream. If so, is similar diurnal precipitation variability also found over  
97 the Kuroshio in the East China Sea? Can prominent diurnal precipitations be found in WBCs in the  
98 Southern Hemisphere? Minobe et al. (2010) suggested that for an energetic deep heating mode to exist,  
99 Sea-Surface Temperature (SST) warmer than 24–26°C may be necessary, and further suggested that the  
100 absence of the deep heating mode (i.e. as strong as over the Gulf Stream) for the WBCs in the Southern  
101 Hemisphere due to the relatively cold SSTs in those regions.

102 The purpose of the present paper is, therefore, to investigate diurnal variability of precipitations  
103 over mid-latitude WBCs. For this purpose, we analyze a satellite-derived precipitation dataset globally in  
104 order to investigate the overall connection of diurnal variations to the WBCs and also regionally to  
105 determine the detailed spatio-temporal structures. The rest of the present paper is organized as follows. In  
106 section 2, we describe the datasets and analysis method. In section 3, diurnal precipitations are analyzed  
107 globally. This global analysis indeed reveals strong diurnal precipitation variability in summer over the  
108 Gulf Stream and over the Kuroshio in the East China Sea. Thus, in the following two sections (section 4  
109 and 5), we conduct closer analyses for these two regions. Discussion and conclusions are presented in  
110 section 6.

111

112

## 113 2. Data and method

114 We analyzed a satellite-derived precipitation dataset and an OLR dataset. The precipitation  
115 dataset is GSMaP MVK version 5 (Ushio et al. 2009). The rain rates in this dataset are estimated using a  
116 Kalman filter from multiple micro-wave satellites combined with an infra-red (IR) dataset provided by  
117 National Oceanic and Atmospheric Administration–Climate Prediction Center (NOAA–CPC), and are

118 provided on an hourly,  $0.1^\circ \times 0.1^\circ$  grid from March 2000 to December 2010. The IR data are used for  
119 moving vectors of estimated precipitation and also for the estimation of the precipitation itself from  
120 brightness temperatures. It should be noted that most of the previous studies of diurnal precipitation used  
121 the TRMM 3B42 dataset, which is on a three-hourly  $0.25^\circ \times 0.25^\circ$  grid (Huffman et al. 2007), whereas the  
122 GSMaP MVK has higher spatial and temporal resolutions than that.

123 We also analyzed a global 3-hourly,  $1^\circ \times 1^\circ$  OLR dataset of NASA/GEWEX Surface Radiation  
124 Budget (SRB) project (Stackhouse et al. 2004). This dataset is available from NASA Langley Research  
125 Center's Atmospheric Science Data Center for a period from July 1982 to December 2007, and analyzed in  
126 this study from 2000 to 2007. The data was briefly analyzed by Minobe et al. (2008), who reported frequent  
127 daytime high cloud occurrence along the Gulf Stream based on occurrence frequency of OLR levels lower  
128 than  $160 \text{ W/m}^2$ , which roughly corresponds to a cloud-top height of about 300 hPa. Following their  
129 approach, we also examine occurrence rate of OLR smaller than  $160 \text{ W/m}^2$  as a measure of high cloud  
130 frequency. In order to know whether the major features found in the OLR-based high cloud frequency are  
131 consistent with independent cloud data, we also examine cloud amount for high-level clouds of D2 dataset  
132 of International Satellite Cloud Climatology Project (ISCCP) for a period from 2000 to 2009 (Rossow and  
133 Schiffer 1999). Spatial resolution D2 dataset is  $2.5^\circ \times 2.5^\circ$ , coarser than that of OLR, with the 3-hourly  
134 sampling interval. High-level clouds in ISCCP D2 dataset are defined clouds that have cloud top pressures  
135 are smaller than 440 hPa, and thus include lower clouds than those used for OLR-based high-cloud  
136 frequency.

137 Diurnal climatologies are calculated for each month and also for each season, and from these the  
138 diurnal amplitude and phase of the 24-hour Fourier component are estimated. The phase is expressed by the  
139 local solar time (LST) for the maximum of this Fourier component, where LST is calculated from  
140 coordinated universal time (UTC) with longitudinal distance between each grid point and  $0^\circ$ . Also, we  
141 examine relative amplitude, given by the amplitude divided by the mean value. If diurnal variability  
142 consists of pure sinusoidal wave of 24-hour component, relative amplitude is in a range between 0 to 100%.  
143 In this case, a relative amplitude of 100% means that the daily minimum is 0% and the maximum is 200%  
144 of the mean value. A relative amplitude can be larger than 100%, when precipitation occur in a narrower  
145 time range than that expected from a sinusoidal wave.

146 In order to show geographical relations between atmospheric and oceanic structures, we also use  
147 climatological satellite-derived SST and surface geostrophic current velocity data. SST data used for  
148 calculating climatological SSTs are optimal interpolation SST ver. 2 on a daily,  $0.25^\circ \times 0.25^\circ$  grid (Reynolds  
149 et al. 2007). Weekly surface geostrophic current velocities, estimated from satellite altimeter, are provided  
150 by AVISO on a  $1/3^\circ \times 1/3^\circ$  grid ([http://www.aviso.oceanobs.com/en/data/product-information/duacs/  
151 ssaltoduacs-products.html](http://www.aviso.oceanobs.com/en/data/product-information/duacs/ssaltoduacs-products.html)).

152

### 153 3. Global view

154 Before analyzing the global diurnal cycles, in order to get some idea of precipitation and  
155 evaporation distributions associated with mid-latitude WBCs, global maps of annual mean rain rate and  
156 evaporations are shown in Fig. 1. Previous studies examined these parameters associated with WBCs over

157 the Northern Hemisphere (Minobe et al. 2008, 2010; Tokinaga et al. 2009; Sasaki et al. 2012) but did not  
158 compare them with those in the Southern Hemisphere. Evaporation data is taken from satellite-derived data  
159 set Japanese Ocean Flux (J-Ofuro) dataset version 2.1 (Kubota and Tomita 2007) for a period from 2000 to  
160 2006. For comparison of the precipitation and evaporation with the geographic locations of the WBCs, the  
161 absolute value of the surface geostrophic velocity is also shown in the figure. In addition to regions of  
162 strong rain rate over the tropics including the inter-tropical convergence zone (ITCZ) and the South Pacific  
163 convergence zone (SPCZ), enhanced rain also occurs over the Gulf Stream, the Kuroshio and the Kuroshio  
164 Extension, consistent with previous observational studies (Minobe et al., 2008; 2010; Tokinaga et al. 2009;  
165 Xu et al. 20012; Sasaki et al. 2013). These mid-latitude precipitation bands are accompanied by enhanced  
166 local evaporation, in contrast to the relatively weak local evaporation in the tropical convergence zones.  
167 Over the Agulhas Return Current, slightly enhanced evaporation and precipitation is found, though the  
168 structure of the latter is somewhat noisy. The enhanced precipitation and accompanying atmospheric  
169 heating can be related to the relatively deep penetration of the oceanic influence on the troposphere in this  
170 region (Liu et al. 2007; Shimada and Minobe 2012). The magnitude of precipitation over the Agulhas  
171 Return Current, however, is much smaller than that over the WBCs in the Northern Hemisphere. In the  
172 Brazil/Malvinas confluence region in the western South Atlantic, the evaporation peaks along the poleward  
173 flowing Brazil current, but no corresponding precipitation band is observed. The strong rainbands over the  
174 Northern Hemisphere WBCs, and weak rainband over the Agulhas Return Current are also seen in the  
175 National Centers for Environmental Prediction (NCEP)-Climate Forecast System Reanalysis (CFSR)  
176 dataset (Saha et al. 2010).

177 Diurnal precipitation amplitudes derived from GSMaP MVK dataset are now examined for each  
178 season. Figure 2a shows that diurnal amplitudes of precipitation are strong over the Gulf Stream and the  
179 Kuroshio in the East China Sea and south of Japan over mid-latitude (poleward of 25°N/S) oceans in boreal  
180 summer, in addition to widely known strong diurnal precipitation in the tropics near lands and in the ITCZ  
181 and SPCZ. The maximal amplitudes reach 0.2 mm/hr over both the Gulf Stream and the Kuroshio.

182 The relative amplitudes (see section 2) of the diurnal precipitation over the Gulf Stream are about  
183 40-70%, and over the Kuroshio are 30-60% (Fig. 2b). These values are much higher than general values,  
184 found to be 10–30% over much of the ocean (Dai et al. 2007). The relative amplitudes over the Gulf Stream  
185 and the Kuroshio indicate a possibility that the diurnal cycle of precipitation in these regions provides an  
186 important contribution to the mean rain rate.

187 Figure 2c shows phases at which the 24-hour precipitation component reaches its maximum in  
188 LST. A prominent feature is the contrasting phase over land and ocean. It is known that the diurnal cycle  
189 tends to have its maximum over the ocean in local morning, while over land it peaks in the local afternoon  
190 to evening (e.g., Dai et al. 2007; Kikuchi and Wang 2008). The phases over the Northern Hemisphere  
191 WBCs follow these general tendencies.

192 In boreal winter, diurnal precipitations in mid-latitude oceans are generally weak, especially over  
193 the mid-latitude WBCs (Fig. 3a). Moderately strong amplitudes are found over a region roughly  
194 corresponding to the North Pacific storm track (Hoskins and Hodges 2002), but corresponding relative  
195 amplitudes are generally smaller than 30% (Fig. 3b). In the Southern Hemisphere, moderately large

196 amplitudes  $\sim 0.06$  mm/hr are found off Brazil in the South Atlantic, with the phases indicating a peak  
197 around noon (Fig. 3c). Although the diurnal cycles in the North Pacific and in the South Atlantic during  
198 boreal winter could be an interesting research subject in its own right, it falls beyond the scope of this paper,  
199 focusing as we do on diurnal cycles over the mid-latitude WBCs. Furthermore, amplitudes and relative  
200 amplitudes of these diurnal precipitation cycles are weaker than those found over the Northern Hemisphere  
201 WBCs in summer (Fig. 2). Therefore, we focus our attention on the diurnal variations over the Gulf Stream  
202 and the Kuroshio in boreal summer, closely examining their spatio-temporal structures in the following  
203 sections.

204

205

#### 206 4. Gulf Stream analysis

207 Figure 4 shows climatological diurnal precipitation amplitudes, along with mean rain rate, over  
208 the Gulf Stream region in June, July and August. As reported by Minobe et al. (2010), who analyzed  
209 summer average precipitation, mean rain rate is enhanced over the Gulf Stream current axis. For convenient  
210 comparison, the spatial structure of the Gulf Stream is shown in Fig. 5. The monthly analysis indicates that  
211 the mean precipitation is especially strong in July, when the Gulf Stream rainband extends further east than  
212 in the other two months. The diurnal amplitudes are also strong over the Gulf Stream for all three months,  
213 with the maximum in July, but appear less well organized than the mean rain rate. The distribution of the  
214 strong diurnal amplitudes is also seen to be contracted westward compared with the spatial structure of the  
215 mean rain band. It is noteworthy that there are two local amplitude maxima in July; one occurs before the  
216 separation of the Gulf Stream from the coast (around  $32^{\circ}\text{N}$ ,  $77^{\circ}\text{W}$ ), and the other after it (around  $36^{\circ}\text{N}$ ,  
217  $70^{\circ}\text{W}$ ). The diurnal precipitation amplitudes over land are larger than those over the ocean, though  
218 magnitudes of mean rain rate over the ocean and land are comparable in June and August or are larger over  
219 the ocean in July. Although the strength of mean Gulf Stream rainband and the amplitudes of diurnal cycle  
220 are strongest in July, their spatial structures are similar during the three months in summer. This is in  
221 marked contrast to the Kuroshio region, where month-to-month changes of spatial patterns are quite large  
222 as will be shown later. In the rest of this section, we describe diurnal variability over the Gulf Stream in  
223 July, when the maximal diurnal precipitation amplitude is observed.

224 The spatial structure of relative amplitudes is not clearly associated with the Gulf Stream (Fig.  
225 6a). Rather, large relative amplitudes (50–90%) are found on and to the east of the Gulf Stream, over SSTs  
226 higher than about  $26^{\circ}\text{C}$ . This means that diurnal precipitation occurs somewhat ubiquitously in this area  
227 over warm SSTs. Consequently, the large diurnal amplitudes over the Gulf Stream reflect large mean  
228 precipitation, which is an aspect of atmospheric response to the Gulf Stream (Minobe et al. 2010),  
229 combined with high relative amplitudes over warm SSTs not limited to the Gulf Stream. The relative  
230 amplitudes over land exceed 100% from the Florida peninsula to Cape Hatteras. The terrestrial high relative  
231 amplitudes suggest that precipitation occurs in narrower time periods than that expected from a sinusoidal  
232 wave. Indeed, this is the case, as will be shown below.

233 The phase of diurnal precipitation in July over the Gulf Stream (Fig. 6b) indicates that the diurnal  
234 precipitation peaks in the morning (about 5–11 LST). As mentioned previously, this early morning

235 maximum is a common feature of diurnal precipitation cycles over the ocean (Yang and Slingo 2001; Dai et  
236 al. 2007; Kikuchi and Wang 2008). The phase generally increases seaward from the Gulf Stream,  
237 suggesting an southeastward phase propagation, with a phase speed in the range of 10–30 m/s. Seaward  
238 phase propagations of tropical diurnal precipitation cycles were reported in previous studies with speeds of  
239 10–20 m/s, possibly due to gravity waves (Yang and Slingo 2001; Kikuchi and Wang 2008). For the  
240 aforementioned two amplitude maxima, the phase of the off-shore maximum slightly leads that of the  
241 near-shore maximum, indicating that precipitation occurs slightly earlier over the Gulf Stream after the  
242 separation than those before the separation with seaward propagation in respective regions. The phases over  
243 land indicate that the diurnal precipitation tend to peak in the late afternoon and early evening (about 15–19  
244 LST), with phases in the Florida peninsula leading those along the coast north of 32°N.

245 As noted above, the diurnal precipitation cycles over the Gulf Stream and over land have roughly  
246 opposite phases. In light of this, it is natural to consider whether the diurnal precipitation cycle over the  
247 ocean is tightly related to that over land. For example, is diurnal precipitation variability over the Gulf  
248 Stream strongly influenced by the diurnal precipitation over North America? Or are these two diurnal  
249 variations are essentially independent? In order to gain some insight into these questions, we conduct a  
250 lag-correlation analysis using raw precipitation data. Here, lag-correlations at each grid point are calculated  
251 with respect to the area-averaged precipitation time series. Two reference time series are chosen; one is  
252 taken for the aforementioned near-shore diurnal amplitude maximum over the Gulf Stream (31–33°N, 78–  
253 76°W), and the other is taken from a region of strong diurnal precipitation cycle over land, along the same  
254 latitudinal band (31–33°N, 83–81°W). The observed significance of the correlations is estimated based on  
255 lag-correlations of large-lags, where data can be assumed to be uncorrelated. More specifically, we  
256 calculate lag correlations with large lags from 7 to 14 days every 6 hours. In order to examine the  
257 significance at a specific grid point these large-lag correlations  $\pm 5^\circ$  in latitudes and longitudes are collected.  
258 The collected correlations are then sorted in order their absolute correlations. If the observed absolute  
259 correlation is higher than top 5% of the collected large-lag absolute correlations, the observed correlation is  
260 considered to be significant at the 5% significance level. This approach is better than the conventional  
261 theoretical estimation of significance, because raw hourly rain rate does not follow a Gaussian distribution,  
262 which is assumed for the theoretical estimation.

263 Figure 7 shows the lag-correlation at the central latitude of the reference time series (32°N). The  
264 lag-correlations do not show a significant out-of-phase relation between the ocean and land with either the  
265 land or ocean reference time series, indicating that the out-of-phase relationship between their respective  
266 diurnal climatologies in Fig. 6b essentially arises independently. A weak land-leading relation is observed  
267 with +12–18 (-18–12) hour lags Fig. 7a (7b). Combined with the aforementioned afternoon and morning  
268 maxima of land and ocean diurnal precipitation, this relation means that occurrence of land-precipitation in  
269 one afternoon may slightly enhance the precipitation over the Gulf stream in next morning. Consistently,  
270 eastward propagation is seen in the lag-correlations over the ocean. The actual propagation direction is  
271 southeastward with the propagation speed about 5 m/s (not shown). This propagation speed is slower than  
272 the phase velocity estimated from the phase distribution in Fig. 6b. Alliss and Raman (1995) suggested that  
273 wind advection can cause a similar lag relation in cloud fields. Another possible mechanism may be gravity

274 wave propagation (Yang and Slingo 2001; Mapes et al. 2003), but the clarification of the responsible  
275 mechanism is a subject of future study. Another interesting point of Fig. 7 is that positive correlations over  
276 the ocean are persistent during  $\pm 36$  hour lags with the ocean reference time series (Fig. 7b) probably related  
277 to synoptic scale variability, whereas correlations over land with the land reference time series does not  
278 show such persistent tendency but exhibit weak negative correlations around  $\pm 12$  hour lags (Fig. 7a). This  
279 suggests that synoptic scale variability exhibits a stronger influence over the ocean than over land  
280 compared to diurnal cycles.

281 Diurnal variability is also seen in high-level clouds. Mean occurrence frequency of high-level clouds  
282 in July is enhanced along the Gulf Stream (Fig. 8a), consistent with a previous study (Minobe et al., 2008;  
283 2010). Figure 8b shows that diurnal amplitudes of the occurrence frequency are large over the Gulf Stream  
284 west of  $65^\circ\text{W}$ , consistent with the diurnal precipitation amplitudes shown in Fig. 4c. The relative  
285 amplitudes of high cloud frequency (Fig. 8c) are generally larger than those of precipitations (Fig. 6a), as  
286 shown by much wider area of relative amplitudes greater than 90% in the former. This indicates that the  
287 diurnal cycle is more apparent in high cloud frequency than in precipitation, suggesting that deep  
288 convection plays an important role in diurnal cycles. The phases for high cloud frequency (Fig. 8d) are  
289 delayed compared to those of the precipitation (Fig. 6b) by 1-2 hour, but otherwise the overall spatial phase  
290 structure is quite consistent with that of the precipitation, including the southeastward phase propagation  
291 noted above. The time lag between the precipitation and high cloud occurrence may reflect the fact that the  
292 high clouds can be persistent for hours after the convection maximum (e.g., Gray and Jacobson 1977;  
293 Rickenbach et al. 2008). The pattern of amplitudes and phases of high-cloud frequency are generally  
294 consistent with those of high-cloud amount of ISCCP D2 dataset, though collocation between the amplitude  
295 maximum with the Gulf Stream current axis and southeastward phase propagations are not well resolved in  
296 the latter dataset due to coarse resolution (not shown).

297 Diurnal cycles may involve other components than the 24-hour Fourier component, and hence it is  
298 interesting to see diurnal climatology time series at some locations. Figure 9a shows diurnal precipitation  
299 climatology time series at four locations (rectangular regions of  $2^\circ \times 2^\circ$ )<sup>1</sup>. These regions are the  
300 aforementioned off-shore and near-shore diurnal amplitude maxima (blue and red curves, respectively),  
301 east of the Gulf Stream (green curve), and on land (black curve). The time series for the amplitude maxima  
302 exhibit relatively narrow peaks and wide troughs. Consistent with the large relative amplitudes described  
303 above, the difference of magnitude between the peak and the trough are remarkable. The diurnal maximum  
304 rain rate is more than four times (three times) larger than the diurnal minimum at the near-shore (off-shore)  
305 amplitude maximum. The diurnal precipitation peak occurs at 4 LST for  $75^\circ\text{W}$  for the off-shore maximum  
306 and at 8 LST for the near-shore maximum, and time series in regions east of the Gulf Stream exhibit further  
307 phase delay. These peak timings are consistent with the phase distribution of Fig. 6b, as the four-hour time  
308 lag is much larger than the about 30-minutes time difference in LST between these two regions. The time  
309 series over land shows a sharp, narrow peak in the afternoon, and very small rain rate in the morning (0-12

---

<sup>1</sup> Animation of diurnal climatology of rain rate over the Gulf Stream region in July (and also over the Kuroshio region June examined in section 5) is found at author's home page, [http://www.sci.hokudai.ac.jp/~minobe/animation/diurnal\\_precip\\_WBCs/](http://www.sci.hokudai.ac.jp/~minobe/animation/diurnal_precip_WBCs/).

310 LST). The narrow peak combined with almost zero rain rate other times results in the relative amplitude  
311 larger than 100%, as previously mentioned. These features of precipitation are generally shared by time  
312 series for high cloud occurrence rate (Fig. 9b), though phase difference over the ocean is less prominent.

313

314

315

## 316 5. Kuroshio

317 In this section, we describe diurnal cycles of precipitation and high cloud occurrence over the  
318 Kuroshio region. In particular, we focus our attention on similarities to and differences from the diurnal  
319 cycles over the Gulf Stream described in the previous section. An important environmental factor in the  
320 Kuroshio region is the presence of the Baiu-Meiyu rain and cloud bands as introduced in section 1.  
321 Baiu-Meiyu rainband typically begins in the middle of May, slowly moves northwards, and disappears in  
322 July as is somewhat reflected in the monthly mean rain rate (Fig. 10bdf). For example, the maximal rain  
323 rate in June to the south of the Kyushu is embedded in the large-scale Baiu-Meiyu rain/cloud band  
324 extending from southern China to the east of Japan, consistent with Fig. 3 of Sasaki et al. (2012), and  
325 relatively strong precipitation around  $32^{\circ}$ – $40^{\circ}$ N in July is also associated with the Baiu-Meiyu rain band.  
326 Another important factor is that a vast land mass, similar to North America to the west of the Gulf Stream,  
327 does not exist around the Kuroshio. Therefore, a comparison of diurnal cycles between the two regions can  
328 give us some insight into the nature of the diurnal cycles over the WBCs. Again for convenient comparison,  
329 the surface geostrophic currents along with SSTs in June are shown in Fig. 11.

330 The strongest diurnal cycle is found in June over the Kuroshio in the East China Sea (Fig. 10c).  
331 In this month, mean rain rate is also the strongest, consistent with Sasaki et al. (2012) (Fig. 10d). The  
332 maximal diurnal amplitude is as high as 0.36 mm/hr to the west of Ryukyu Islands, which is about 30%  
333 larger than the maximum amplitude during July in the North Atlantic (0.28 mm/hr), and this is the largest  
334 diurnal precipitation amplitude over the mid-latitude global oceans in all calendar months. In June, the  
335 secondary amplitude maximum is seen to the south of Kyushu, and two patches of relatively high  
336 amplitude are found in the North Pacific to the south of Japan. These spatial features are not seen in the  
337 average precipitation, which is more smoothly distributed from the East China Sea to the North Pacific.  
338 The strong diurnal precipitations in the East China Sea are limited to June and not found in either May or  
339 July (Fig. 10ace). This is in contrast to the diurnal cycle over the Gulf Stream, which exhibits similar  
340 spatial structures during all summer months. The rapid month to month transition of diurnal precipitations  
341 is closely related to the mean precipitation change, which is governed by the northward migration of the  
342 Baiu-Meiyu rainband (e.g., Wang and LinHo 2002). In the rest of this section, we closely examine diurnal  
343 cycles over the Kuroshio in June.

344 Despite the strong diurnal precipitation amplitudes over the Kuroshio in the East China Sea, the  
345 relative amplitudes in this region are slightly smaller than those over the Gulf Stream (Fig. 12a). This is  
346 because mean precipitation over the Kuroshio is much larger than that over the Gulf Stream, and the  
347 maximum mean rain rate of the former region is about two times larger than the latter (Note that maximum  
348 value for the color scale of Fig. 10d is two times larger than that in Fig. 4d). The strong mean precipitation

349 is associated with the large-scale Baiu-Meiyu rain band, in which enhanced precipitation due to the  
350 Kuroshio is located over the East China Sea (Sasaki et al., 2012). The Baiu-Meiyu rain band itself does not  
351 generally exhibit a strong diurnal cycle, as shown by weak relative amplitude south of Japan (Fig 12a).  
352 These results indicate that the combination of the Kuroshio's impact on the diurnal precipitation cycle and  
353 large-scale Baiu-Meiyu rainband with a weak diurnal cycle, is important for understanding the diurnal  
354 variations over the Kuroshio in the East China Sea.

355 Figure 12b shows the phase distribution of the 24-hour components of precipitation over the  
356 Kuroshio region. Peak time for large diurnal amplitudes (say 0.2 mm/hr or more) is 10–13 LST, few hours  
357 later than that over the Gulf Stream. Also, around the large diurnal amplitudes, phases indicate  
358 southeastward increase with the speeds of 10–20 m/s. The propagation direction is roughly the same as that  
359 in the Gulf Stream region, but the propagation speed over the Kuroshio is somewhat slower.

360 Diurnal variability is also found in high cloud occurrence in June over the Kuroshio. Mean high  
361 cloud occurrence (Fig 13a) shows a similar spatial pattern to that of precipitation (Fig. 10d). The magnitude  
362 is again much larger than that over the Gulf Stream, consistent with precipitation. Diurnal amplitudes of  
363 high cloud occurrence exhibits a maximum over the Ryukyu Islands (Fig. 13b), roughly collocated with  
364 high amplitude region of diurnal precipitation variations. However, the location of the maximum high cloud  
365 amplitude is slightly shifted to the east compared to the precipitation maximum, which could be due to  
366 anvils advected by background westerlies. The maximum amplitude (11%) is similar to the maximum value  
367 over the Gulf Stream (10%). Relative amplitudes over the Kuroshio are, on the other hand, much smaller  
368 than those over the Gulf Stream (Figs. 8c, 13c), due to the larger mean high cloud occurrence rates.  
369 Therefore, for both the precipitation and high cloud occurrence, the diurnal component associated with the  
370 Kuroshio and the Gulf Stream have similar magnitudes, but the superimposed large-scale Baiu-Meiyu rain  
371 band without strong diurnal variability results in small relative amplitudes over the Kuroshio region.

372 Phases of the 24-hour component of high cloud occurrence rate exhibit peaks in the early  
373 afternoon (12-16 LST) over regions of strong amplitudes, straddling the East China Sea and the western  
374 North Pacific (Fig. 13d). In this region, phases of high cloud occurrence are delayed by 2-3 hours compared  
375 with those of precipitation, and this delay is slightly longer than is found over the Gulf Stream. An  
376 southeastward phase propagation is found for the large amplitude region, consistent with precipitation. The  
377 phase and amplitude distributions of high-cloud frequency derived from OLR data are generally consistent  
378 with those of high-cloud amount of ISCCP D2 dataset (not shown).

379 Figure 14 shows diurnal climatology time series of precipitation and high-cloud occurrence rate  
380 at three locations around the diurnal precipitation amplitude maximum. Consistent with the aforementioned  
381 phase propagation, the time at which the diurnal precipitation peak occurs is increasingly delayed in the  
382 southeastward direction (Fig. 14a). Interestingly, the peak of high-cloud frequency in the region of the  
383 precipitation amplitude maximum occurs in evening, 18 LST, delayed by about 8 hours compared to the  
384 precipitation peak (Fig. 14b). The reason why the peak time difference in the East China Sea is much larger  
385 than that over the Gulf Stream is not known to the authors, and is a potential subject of future study.

386

## 387 6. Discussion and conclusions

388 Diurnal variations over the mid-latitude oceans are analyzed using an hourly, satellite-derived  
389 precipitation dataset (GSMaP MVK ver. 5) and 3-hourly OLR data from the SRB project. Previous studies  
390 have also described diurnal precipitation cycles, including the mid-latitude oceans (e.g., Dai et al. 2007),  
391 although the link between diurnal precipitation cycles and WBCs is analyzed comprehensively in this study.  
392 It is found that over mid-latitude oceans, poleward of 25°N/S, strong diurnal cycles occur over the Northern  
393 Hemisphere WBCs, i.e., the Gulf Stream and the Kuroshio, in the boreal summer season (Fig. 2). No  
394 prominent diurnal precipitation is found over the WBCs in the Southern Hemisphere the whole year round  
395 (Figs. 2 and 3).

396 There are some common features but also differences in the diurnal cycles between the regions  
397 over the Gulf Stream and the Kuroshio. In both regions, maximum amplitudes of diurnal precipitation  
398 occur roughly over the current axes with a pattern contracted westward compared with the rainbands, more  
399 specifically, just before and after the separation at the Cape Hatteras for the Gulf Stream (Fig. 4) and west  
400 of Ryukyu Islands in the East China Sea for the Kuroshio (Fig. 10). The maximum amplitudes are slightly  
401 larger over the Kuroshio than over the Gulf Stream. The diurnal phases commonly exhibit southeastward  
402 propagation, with peak times for the large amplitudes being from early to late morning (5-11 LST) for the  
403 Gulf Stream (Fig. 6b) and from late morning to noon (10-13 LST) over the Kuroshio in the East China Sea  
404 (Fig. 12b). Occurrence frequencies of high clouds exhibit diurnal cycles consistent with those of the  
405 precipitation. The relative amplitudes of high cloud occurrence are larger than those of precipitation,  
406 suggesting that the diurnal precipitation is mainly due to deep convection, consistent with studies of  
407 tropical diurnal precipitation over the oceans (e.g., Janowiak et al. 1994; Yang and Slingo 2001). Near the  
408 Gulf Stream, diurnal precipitation cycles over North America are roughly 180° out-of-phase of those over  
409 the ocean (Fig. 6b). The lag-correlation analysis shows that a direct link between oceanic and terrestrial  
410 diurnal cycles is not strong (Fig. 7), if it exists at all, and thus they probably originate different physical  
411 mechanisms.

412 Major differences between the diurnal cycles over the Gulf Stream and those over the Kuroshio  
413 are likely to be associated with the presence of large-scale Baiu-Meiyu rainband, consistent with Sasaki et  
414 al. (2012) who suggested that local atmospheric response to the Kuroshio in the East China Sea is  
415 embedded in large-scale Baiu-Meiyu rainband. The seasonal northward migration of Baiu-Meiyu rainband,  
416 associated with development of the subtropical high, yields substantially different diurnal precipitations  
417 from a month to month. The prominent diurnal precipitation is limited to June (Fig. 10), the peak month of  
418 the Baiu-Meiyu precipitation over the East China Sea. On the other hand, the spatial patterns of the diurnal  
419 and mean precipitation over the Gulf Stream do not change much from June to August, with the maximum  
420 amplitude occurring during July (Fig. 4). The maximum mean rain rate over the Kuroshio in the East China  
421 Sea and south of Japan in June is roughly two times larger than that over the Gulf Stream in July (Figs. 4,  
422 10). The large mean rain rate associated with the Baiu-Meiyu rainband results in smaller relative  
423 amplitudes over the Kuroshio than are found over the Gulf Stream (Figs. 6a, 12a). The large relative  
424 amplitudes of precipitation and high cloud occurrence are widely distributed over warm SSTs in the North  
425 Atlantic. Large relative amplitudes over the Kuroshio region, however, are only found in the vicinity of the

426 Kuroshio itself. This does not necessary mean that diurnal precipitations do not occur over a wider area, but  
427 if they occur, they may be obscured by the large-scale Baiu-Meiyu rainband in which prominent diurnal  
428 cycles are absent. Major features of the diurnal precipitation and high cloud cycles are summarized in Fig.  
429 15.

430 The diurnal cycles are likely to be closely associated with the deep heating mode of the  
431 atmospheric response to the WBCs. The spatial and seasonal distributions of the strong deep heating mode  
432 found in previous studies (Minobe et al. 2010; Sasaki et al. 2012) and those of diurnal precipitation appear  
433 to be similar to one another. This is not surprising, because as discussed in section 1, it is known that  
434 diurnal precipitation variability is strong in the tropics, and the deep heating mode is a tropical-like  
435 atmospheric response to ocean fronts over SSTs warmer than 24–26°C (Minobe et al., 2010). It is  
436 noteworthy that diurnal precipitation variability over the Gulf Stream and the Kuroshio has higher relative  
437 amplitudes than those over most of the tropics. Furthermore, contributions of diurnal cycles to average rain  
438 rate are larger over the WBCs than in the ITCZ and SPCZ, and thus diurnal variability can be an important  
439 agent for producing in mean precipitations in the WBC regions. Consequently, it is strongly suggested that  
440 the diurnal precipitation and cloud cycles are intrinsic and important aspects of the deep heating mode.

441 A natural question is what mechanism is responsible for the diurnal cycles over the Gulf Stream  
442 and the Kuroshio? This is an open question not only for the diurnal cycles over these WBCs but also for  
443 diurnal cycles over the tropical oceans, which have been much more widely studied (e.g., Dai et al. 2007;  
444 Kikuchi and Wang 2008). Yang and Smith (2006) summarized twelve proposed mechanisms for diurnal  
445 precipitation. Among these mechanisms, a morning maximum may be produced by two mechanisms. One  
446 mechanism is static radiation convection, in which radiative cooling from the top of clouds during the night  
447 time destabilizes the upper cloud, and thus increases convection and precipitation (e.g., Kraus 1963;  
448 Randall et al. 1991). Another mechanism is static radiation convection with enhanced moistening (Tao et al.  
449 1996; Sui et al. 1997). In this mechanism, enhanced night time radiative cooling increases humidity, and  
450 thus amplifies condensation and precipitation. It is interesting to examine whether one of these, or other,  
451 mechanisms play a role over the WBCs in future study. The southeastward phase propagations observed  
452 over the Gulf Stream and East China Sea are somewhat reminiscent of previously reported seaward phase  
453 propagations of diurnal precipitation cycles in the tropics (Yang and Slingo 2001; Kikuchi and Wang 2008).  
454 It is suggested that the tropical seaward phase propagation is due to gravitation waves, which can generated  
455 by topographic effects (Mapes et al. 2003) or land convection (Zuidema 2003). Another possible  
456 mechanism for the phase propagation is advection by background winds, as has been suggested for diurnal  
457 cloud developments over the Gulf Stream region (Alliss and Raman 1995).

458 In order to identify the mechanism, atmospheric numerical models should be useful. Indeed, Fig.  
459 5 of Dirmeyer et al. (2012) shows that enhanced diurnal precipitation over the Gulf Stream are somewhat  
460 reproduced by several numerical models. However, in that paper, which focuses on diurnal precipitations  
461 over North America, phases over the North Atlantic are masked out due to small amplitudes for most of  
462 models, and thus it is not clear whether these models can reproduce the observed phase distribution. A  
463 model whose phase distribution over the western North Atlantic was shown in that paper is  
464 the Nonhydrostatic ICosahedral Atmospheric Model (NICAM), which exhibits reasonable phase difference

465 between the off-shore region and near-shore region along the Gulf Stream, but the seaward phase increase  
 466 is not seen. Nevertheless, a reasonable step for identifying the mechanism for the diurnal cycle in real  
 467 world may be to examine these and other model outputs to assess the degree to which they can reproduce  
 468 the diurnal cycles and to then identify the responsible mechanisms.

469 It should be worth noting that successfully capturing the diurnal cycle in numerical atmospheric  
 470 models can be essential in producing mean realistic distributions of precipitation and thus atmospheric  
 471 heating. Moisture used for the precipitation over the Gulf Stream and the Kuroshio is supplied by the local  
 472 evaporation and moisture transport from the south along the west flank of the Subtropical high (Minobe et  
 473 al., 2010; Sasaki et al., 2012). The diurnal cycle can thus play an essential role in turning the moisture into  
 474 precipitation in the relevant locations. If this hypothesis is correct, numerical model tunings, which  
 475 primarily focus on the diurnal cycle, can improve not only the diurnal cycle itself but also mean  
 476 precipitation distributions. This hypothesis can be examined by changing parameterizations or radiation  
 477 forcings in a model. According to this hypothesis, the diurnal cycle can be important not only in the context  
 478 of weather, but also from a climate perspective. Consequently, the diurnal cycles over the Gulf Stream and  
 479 the Kuroshio, which may be an intrinsic aspect of the deep heating mode, link the ocean and the  
 480 atmosphere, and also possibly weather and climate.

481

## 482 Acknowledgement

483 Many thanks for Dr. C. O'Reilly for comments on the English and also on the science, and for two  
 484 anonymous reviewers for their helpful and constructive comments. This work was supported by the Japan  
 485 Society for the Promotion of Science (Grant-in-Aid for Scientific Research 22106008 and 22244057).

486

## 487 References

- 488 Alexander MA, Scott JD (1997) Surface flux variability over the North Pacific and North  
 489 Atlantic Oceans. *J Climate* 10 (11):2963-2978.  
 490 doi:10.1175/1520-0442(1997)010<2963:sfvotn>2.0.co;2
- 491 Alliss RJ, Raman S (1995) Diurnal-variations in-cloud frequency over the Gulf-Stream locale.  
 492 *Journal of Applied Meteorology* 34 (7):1578-1594.  
 493 doi:10.1175/1520-0450(1995)034<1578:dvicfo>2.0.co;2
- 494 Booth JF, Thompson L, Patoux J, Kelly KA (2012) Sensitivity of Midlatitude Storm  
 495 Intensification to Perturbations in the Sea Surface Temperature near the Gulf Stream.  
 496 *Mon Wea Rev* 140 (4):1241-1256. doi:10.1175/mwr-d-11-00195.1
- 497 Booth JF, Thompson L, Patoux J, Kelly KA, Dickinson S (2010) The signature of the  
 498 midlatitude tropospheric storm tracks in the surface winds. *J Climate* 23 (5):1160-1174.  
 499 doi:10.1175/2009jcli3064.1
- 500 Brayshaw DJ, Hoskins B, Blackburn M (2008) The storm-track response to idealized SST  
 501 perturbations in an aquaplanet GCM. *J Atmos Sci* 65 (9):2842-2860.  
 502 doi:10.1175/2008jas2657.1
- 503 Brayshaw DJ, Hoskins B, Blackburn M (2011) The basic ingredients of the North Atlantic

- 504 storm track. Part II: sea surface temperatures. *J Atmos Sci* 68 (8):1784-1805. doi:Doi  
505 10.1175/2011jas3674.1
- 506 Chelton DB, Schlax MG, Freilich MH, Milliff RF (2004) Satellite measurements reveal  
507 persistent small-scale features in ocean winds. *Science* 303 (5660):978-983.  
508 doi:10.1126/science.1091901
- 509 Chelton DB, Xie SP (2010) Coupled ocean-atmosphere interaction at oceanic mesoscales.  
510 *Oceanography* 23 (4):52-69
- 511 Czaja A, Blunt N (2011) A new mechanism for ocean-atmosphere coupling in midlatitudes.  
512 *Quart J Roy Meteor Soc* 137 (657):1095-1101. doi:10.1002/qj.814
- 513 Dai A, Lin X, Hsu K-L (2007) The frequency, intensity, and diurnal cycle of precipitation in  
514 surface and satellite observations over low- and mid-latitudes. *Clim Dyn* 29  
515 (7-8):727-744. doi:10.1007/s00382-007-0260-y
- 516 Dirmeyer PA, Cash BA, Kinter JL, Jung T, Marx L, Satoh M, Stan C, Tomita H, Towers P,  
517 Wedi N, Achuthavarier D, Adams JM, Altshuler EL, Huang BH, Jin EK, Manganello J  
518 (2012) Simulating the diurnal cycle of rainfall in global climate models: resolution  
519 versus parameterization. *Clim Dyn* 39 (1-2):399-418. doi:10.1007/s00382-011-1127-9
- 520 Gray WM, Jacobson RW (1977) Diurnal-variation of deep cumulus convection. *Mon Wea*  
521 *Rev* 105 (9):1171-1188. doi:10.1175/1520-0493(1977)105<1171:dvodcc>2.0.co;2
- 522 Hayasaki M, Kawamura R, Mori M, Watanabe M (2013) Response of extratropical cyclone  
523 activity to the Kuroshio large meander in northern winter. *Geophys Res Lett* 40  
524 (11):2851-2855. doi:10.1002/grl.50546
- 525 Hoskins BJ, Hodges KI (2002) New perspectives on the Northern Hemisphere winter storm  
526 tracks. *J Atmos Sci* 59 (6):1041-1061. doi:Doi  
527 10.1175/1520-0469(2002)059<1041:Npotnh>2.0.Co;2
- 528 Hoskins BJ, McIntyre ME, Robertson AW (1985) On the use and significance of isentropic  
529 potential vorticity maps. *Quart J Roy Meteor Soc* 111 (470):877-946.  
530 doi:10.1256/smsqj.47001
- 531 Hoskins BJ, Valdes PJ (1990) On the existence of storm-tracks. *J Atmos Sci* 47  
532 (15):1854-1864. doi:Doi 10.1175/1520-0469(1990)047<1854:Oteost>2.0.Co;2
- 533 Huffman GJ, Adler RF, Bolvin DT, Gu GJ, Nelkin EJ, Bowman KP, Hong Y, Stocker EF,  
534 Wolff DB (2007) The TRMM multisatellite precipitation analysis (TMPA):  
535 Quasi-global, multiyear, combined-sensor precipitation estimates at fine scales.  
536 *Journal of Hydrometeorology* 8 (1):38-55. doi:10.1175/jhm560.1
- 537 Inatsu M, Hoskins BJ (2004) The zonal asymmetry of the Southern Hemisphere winter storm  
538 track. *J Climate* 17 (24):4882-4892. doi:10.1175/jcli-3232.1
- 539 Inatsu M, Mukougawa H, Xie SP (2003) Atmospheric response to Zonal variations in  
540 midlatitude SST: Transient and stationary eddies and their feedback. *J Climate* 16  
541 (20):3314-3329. doi:10.1175/1520-0442(2003)016<3314:artzvi>2.0.co;2
- 542 Janowiak JE, Arkin PA, Morrissey M (1994) An examination of the diurnal cycle in oceanic

- 543 tropical rainfall using satellite and in-situ data. *Mon Wea Rev* 122 (10):2296-2311.  
544 doi:10.1175/1520-0493(1994)122<2296:aeotdc>2.0.co;2
- 545 Joyce TM, Kwon Y-O, Yu L (2009) On the relationship between synoptic wintertime  
546 atmospheric variability and path shifts in the Gulf Stream and the Kuroshio Extension.  
547 *J Climate* 22 (12):3177-3192. doi:10.1175/2008jcli2690.1
- 548 Kikuchi K, Wang B (2008) Diurnal precipitation regimes in the global tropics. *J Climate* 21  
549 (11):2680-2696. doi:10.1175/2007jcli2051.1
- 550 Kraus EB (1963) The diurnal precipitation change over the sea. *J Atmos Sci* 20 (6):551-556.  
551 doi:10.1175/1520-0469(1963)020<0551:tdpcot>2.0.co;2
- 552 Kubota M, Tomita H (2007) The present state of the J-OFURO air-sea interaction data  
553 product. *Flux News*. WCRP,
- 554 Kuo YH, Shapiro MA, Donall EG (1991) The interaction between baroclinic and diabatic  
555 processes in a numerical-simulation of a rapidly intensifying extratropical marine  
556 cyclone. *Mon Wea Rev* 119 (2):368-384.  
557 doi:10.1175/1520-0493(1991)119<0368:tibbad>2.0.co;2
- 558 Kuwano-Yoshida A, Minobe S, Xie S-P (2010) Precipitation response to the Gulf Stream in  
559 an atmospheric GCM. *J Climate* 23 (13):3676-3698. doi:10.1175/2010jcli3261.1
- 560 Liu WT, Xie X, Niiler PP (2007) Ocean-atmosphere interaction over agulhas extension  
561 meanders. *J Climate* 20 (23):5784-5797. doi:10.1175/2007jcli1732.1
- 562 Mapes BE, Warner TT, Xu M (2003) Diurnal patterns of rainfall in northwestern South  
563 America. Part III: Diurnal gravity waves and nocturnal convection offshore. *Mon Wea*  
564 *Rev* 131 (5):830-844. doi:10.1175/1520-0493(2003)131<0830:dporin>2.0.co;2
- 565 Minobe S, Kuwano-Yoshida A, Komori N, Xie S-P, Small RJ (2008) Influence of the Gulf  
566 Stream on the troposphere. *Nature* 452 (7184):206-U251. doi:10.1038/nature06690
- 567 Minobe S, Miyashita M, Kuwano-Yoshida A, Tokinaga H, Xie S-P (2010) Atmospheric  
568 response to the Gulf Stream: Seasonal variations. *J Climate* 23 (13):3699-3719.  
569 doi:10.1175/2010jcli3359.1
- 570 Nakamura H, Nishina A, Minobe S (2012) Response of storm tracks to bimodal Kuroshio  
571 path states south of Japan. *J Climate* 25 (21):7772-7779.  
572 doi:10.1175/jcli-d-12-00326.1
- 573 Nakamura H, Sampe T, Goto A, Ohfuchi W, Xie S-P (2008) On the importance of midlatitude  
574 oceanic frontal zones for the mean state and dominant variability in the tropospheric  
575 circulation. *Geophys Res Lett* 35 (15). doi:10.1029/2008gl034010
- 576 Nakamura H, Sampe T, Tanimoto Y, Simpo A (2004) Observed associations among storm  
577 tracks, jet streams and midlatitude oceanic fronts. . In: Wang C, Xie SP, Carton JA  
578 (eds) *Earth Climate: The ocean-atmosphere interaction*, *Geophys. Monogr.*, vol 147.  
579 Amer. Geophys. Union, pp 329-345
- 580 Nesbitt SW, Zipser EJ (2003) The diurnal cycle of rainfall and convective intensity according  
581 to three years of TRMM measurements. *J Climate* 16 (10):1456-1475.

- 582 doi:10.1175/1520-0442-16.10.1456
- 583 Ninomiya K, Akiyama T (1992) Multiscale features of baiu, the summer monsoon over Japan  
584 and the East-Asia. *J Meteor Soc Japan* 70 (1B):467-495
- 585 Nonaka M, Nakamura H, Taguchi B, Komori N, Kuwano-Yoshida A, Takaya K (2009)  
586 Air-sea heat exchanges characteristic of a prominent midlatitude oceanic front in the  
587 South Indian Ocean as simulated in a high-resolution coupled GCM. *J Climate* 22  
588 (24):6515-6535. doi:10.1175/2009jcli2960.1
- 589 Ogawa F, Nakamura H, Nishii K, Miyasaka T, Kuwano-Yoshida A (2012) Dependence of the  
590 climatological axial latitudes of the tropospheric westerlies and storm tracks on the  
591 latitude of an extratropical oceanic front. *Geophys Res Lett* 39.  
592 doi:10.1029/2011gl049922
- 593 Oki T, Musiaka K (1994) Seasonal change of the diurnal cycle of precipitation over Japan and  
594 malaysia. *Journal of Applied Meteorology* 33 (12):1445-1463.  
595 doi:10.1175/1520-0450(1994)033<1445:scotdc>2.0.co;2
- 596 Randall DA, Harshvardhan, Dazlich DA (1991) Diurnal variability of the hydrologic-cycle in  
597 a general-circulation model. *J Atmos Sci* 48 (1):40-62.  
598 doi:10.1175/1520-0469(1991)048<0040:dvothc>2.0.co;2
- 599 Reynolds RW, Smith TM, Liu C, Chelton DB, Casey KS, Schlax MG (2007) Daily  
600 high-resolution-blended analyses for sea surface temperature. *J Climate* 20  
601 (22):5473-5496. doi:10.1175/2007jcli1824.1
- 602 Rickenbach T, Kucera P, Gentry M, Carey L, Lare A, Lin RF, Demoz B, Starr DO (2008) The  
603 relationship between anvil clouds and convective cells: A case study in South Florida  
604 during CRYSTAL-FACE. *Mon Wea Rev* 136 (10):3917-3932.  
605 doi:10.1175/2008mwr2441.1
- 606 Rossow WB, Schiffer RA (1999) Advances in understanding clouds from ISCCP. *Bull Amer*  
607 *Meteor Soc* 80 (11):2261-2287.  
608 doi:10.1175/1520-0477(1999)080<2261:aiucfi>2.0.co;2
- 609 Rudeva I, Gulev SK (2011) Composite analysis of North Atlantic extratropical cyclones in  
610 NCEP-NCAR reanalysis data. *Mon Wea Rev* 139 (5):1419-1446.  
611 doi:10.1175/2010mwr3294.1
- 612 Saha S, Moorthi S, Pan HL, Wu XR, Wang JD, Nadiga S, Tripp P, Kistler R, Woollen J,  
613 Behringer D, Liu HX, Stokes D, Grumbine R, Gayno G, Wang J, Hou YT, Chuang HY,  
614 Juang HMH, Sela J, Iredell M, Treadon R, Kleist D, Van Delst P, Keyser D, Derber J,  
615 Ek M, Meng J, Wei HL, Yang RQ, Lord S, Van den Dool H, Kumar A, Wang WQ,  
616 Long C, Chelliah M, Xue Y, Huang BY, Schemm JK, Ebisuzaki W, Lin R, Xie PP,  
617 Chen MY, Zhou ST, Higgins W, Zou CZ, Liu QH, Chen Y, Han Y, Cucurull L,  
618 Reynolds RW, Rutledge G, Goldberg M (2010) THE NCEP CLIMATE FORECAST  
619 SYSTEM REANALYSIS. *Bull Amer Meteor Soc* 91 (8):1015-1057.  
620 doi:10.1175/2010bams3001.1

- 621 Sampe T, Xie SP (2007) Mapping high sea winds from space: A global climatology. Bull  
622 Amer Meteor Soc 88 (12):1965-+. doi:10.1175/bams-88-12-1965
- 623 Sampe T, Xie SP (2010) Large-Scale dynamics of the Meiyu-Baiu rainband: Environmental  
624 forcing by the westerly jet. J Climate 23 (1):113-134. doi:10.1175/2009jcli3128.1
- 625 Sasaki YN, Minobe S, Asai T, Inatsu M (2012) Influence of the Kuroshio in the East China  
626 Sea on the early summer (Baiu) rain. J Climate 25 (19):6627-6645.  
627 doi:10.1175/jcli-d-11-00727.1
- 628 Shaman J, Samelson RM, Skillingstad E (2010) Air-sea fluxes over the Gulf Stream region:  
629 Atmospheric controls and trends. J Climate 23 (10):2651-2670.  
630 doi:10.1175/2010jcli3269.1
- 631 Shimada T, Minobe S (2011) Global analysis of the pressure adjustment mechanism over sea  
632 surface temperature fronts using AIRS/Aqua data. Geophys Res Lett 38.  
633 doi:10.1029/2010gl046625
- 634 Small RJ, deSzoeko SP, Xie SP, O'Neill L, Seo H, Song Q, Cornillon P, Spall M, Minobe S  
635 (2008) Air-sea interaction over ocean fronts and eddies. Dynamics of Atmospheres  
636 and Oceans 45 (3-4):274-319. doi:10.1016/j.dynatmoce.2008.01.001
- 637 Stackhouse PW, Gupta SK, Cox SJ, Colleen MJ, Zhang T, Chiacchio M (2004) Twelve-year  
638 surface radiation budget data set. GEWEX News 14 (4):10-12
- 639 Sui CH, Lau KM, Takayabu YN, Short DA (1997) Diurnal variations in tropical oceanic  
640 cumulus convection during TOGA COARE. J Atmos Sci 54 (5):639-655.  
641 doi:10.1175/1520-0469(1997)054<0639:dvitoc>2.0.co;2
- 642 Taguchi B, Nakamura H, Nonaka M, Xie S-P (2009) Influences of the Kuroshio/Oyashio  
643 Extensions on Air-Sea Heat Exchanges and Storm-Track Activity as Revealed in  
644 Regional Atmospheric Model Simulations for the 2003/04 Cold Season. J Climate 22  
645 (24):6536-6560. doi:10.1175/2009jcli2910.1
- 646 Tao WK, Lang S, Simpson J, Sui CH, Ferrier B, Chou MD (1996) Mechanisms of  
647 cloud-radiation interaction in the tropics and midlatitudes. J Atmos Sci 53  
648 (18):2624-2651. doi:10.1175/1520-0469(1996)053<2624:mocrii>2.0.co;2
- 649 Tokinaga H, Tanimoto Y, Xie S-P, Sampe T, Tomita H, Ichikawa H (2009) Ocean frontal  
650 effects on the vertical development of clouds over the western North Pacific: In situ  
651 and satellite observations. J Climate 22 (16):4241-4260. doi:10.1175/2009jcli2763.1
- 652 Ushio T, Sasashige K, Kubota T, Shige S, Okamoto K, Aonashi K, Inoue T, Takahashi N,  
653 Iguchi T, Kachi M, Oki R, Morimoto T, Kawasaki ZI (2009) A Kalman filter approach  
654 to the global satellite mapping of precipitation (GSMaP) from combined passive  
655 microwave and infrared radiometric data. J Meteor Soc Japan 87:137-151.  
656 doi:10.2151/jmsj.87A.137
- 657 Wallace JM (1975) Diurnal-variations in precipitation and thunderstorm frequency over  
658 conterminous united-states. Mon Wea Rev 103 (5):406-419.  
659 doi:10.1175/1520-0493(1975)103<0406:dvipat>2.0.co;2

- 660 Wang B, LinHo (2002) Rainy season of the Asian-Pacific summer monsoon. *J Climate* 15  
661 (4):386-398. doi:10.1175/1520-0442(2002)015<0386:rsotap>2.0.co;2
- 662 Xie SP (2004) Satellite observations of cool ocean-atmosphere interaction. *Bull Amer Meteor*  
663 *Soc* 85 (2):195-+. doi:10.1175/bams-85-2-195
- 664 Xu HM, Xu MM, Xie SP, Wang YQ (2011) Deep atmospheric response to the spring  
665 Kuroshio over the East China Sea. *J Climate* 24 (18):4959-4972.  
666 doi:10.1175/jcli-d-10-05034.1
- 667 Yang GY, Slingo J (2001) The diurnal cycle in the Tropics. *Mon Wea Rev* 129 (4):784-801.  
668 doi:10.1175/1520-0493(2001)129<0784:tdcitt>2.0.co;2
- 669 Zolina O, Gulev SK (2003) Synoptic variability of ocean-atmosphere turbulent fluxes  
670 associated with atmospheric cyclones. *J Climate* 16 (16):2717-2734.  
671 doi:10.1175/1520-0442(2003)016<2717:svoottf>2.0.co;2
- 672 Zuidema P (2003) Convective clouds over the Bay of Bengal. *Mon Wea Rev* 131 (5):780-798.  
673 doi:10.1175/1520-0493(2003)131<0780:ccotbo>2.0.co;2
- 674
- 675

## 676 Figure Captions

677

678 Fig. 1. Annual mean climatology of a) rain rate from GSMaP MVK from March 2000 to November 2010,  
 679 b) evaporation from the J-Ofuro dataset from January 2000 to December 2006, c) surface geostrophic  
 680 current velocities provided by AVISO from January 2000 to December 2010.

681

682 Fig. 2 a) Amplitude, b) relative amplitude and c) phase of diurnal precipitation cycle in boreal summer  
 683 (June–August). Gray areas over the ocean in panel (a) are excluded from the analysis, because missing data  
 684 rate due to presence of ice is larger than 20%. The values in panels (b, c) are drawn for the region where the  
 685 amplitudes are larger than 0.02 mm/hr. Horizontal lines indicate 25°N/S.

686

687 Fig. 3. Same as Fig. 2, but for the boreal winter (December–February).

688

689 Fig. 4. Amplitudes of 24-hour diurnal cycle (left) and mean rain rate (right) of precipitations over the Gulf  
 690 Stream region in June (top), July (middle) and August (bottom). Gray areas in left panels are excluded from  
 691 the analysis, because missing data rate due to presence of ice is larger than 20%. Contours in each panel  
 692 indicate SSTs with a contour interval of every 2°C and dashed contours for 24° and 26°C.

693

694 Fig. 5. Climatological absolute surface geostrophic velocity derived from satellite altimeter (color) and  
 695 SSTs (contours) with a contour interval of every 2°C and dashed contours for 24° and 26°C in July.

696

697 Fig. 6. a) Relative amplitudes and b) phases of the precipitation diurnal cycle over the Gulf Stream region  
 698 in July. Phases shown by the time of maximum value of 24-hour cycle in LST. Contours indicate 0.1 (thin  
 699 contour) and 0.15 mm/hr (thick contour) of the amplitudes shown in Fig. 4 (c). White regions are either  
 700 missing data, due to presence of ice being larger than 20%, or the amplitudes shown in Fig. 4 (c) are  
 701 smaller than 0.02 mm/hr.

702

703 Fig. 7. Lag correlation coefficients at each grid point along 32.05N onto the reference area-averaged  
 704 precipitation time series (a) in a region 83–81°W, 31–33°N over land and (b) in a region 78–76°W, 31–  
 705 33°N over the ocean. Positive lags indicate reference time series leading to data at each grid point.

706

707 Fig. 8. a) average, b) amplitudes, c) relative amplitudes and d) phases of occurrence rate of high cloud  
 708 estimated from OLR over the Gulf Stream region in July. Phases shown by the time of maximal value of  
 709 24-hour cycle in LST. Contours in panels (a) and (b) are SSTs with a contour interval of 2°C, where dashed  
 710 contours indicate 24° and 26°C, whereas contours in panels (b) and (c) are diurnal amplitudes of 5 and 8 %.

711

712 Fig. 9. Climatological time series of (a) rain rate and (b) high cloud frequency in July averaged over  
 713 different areas. Black line indicates a box over land (31°–33°N, 83°–81°W), blue line indicates a box for  
 714 the off-shore diurnal precipitation maximum (35–37°N, 72–70°W), red line indicates a box for the

715 near-shore diurnal precipitation maximum ( $31^{\circ}$ – $33^{\circ}$ N,  $76^{\circ}$ – $78^{\circ}$ W), and green line indicates a box to the  
716 east of the near-shore maximum (east of the Gulf Stream) ( $31^{\circ}$ – $33^{\circ}$ N,  $72^{\circ}$ – $78^{\circ}$ W).

717

718 Fig. 10. Same as Fig. 4, but for the Kuroshio region in May (top), June (middle) and July (bottom). Note  
719 that the color-scale values are larger than those in Fig. 4.

720

721 Fig. 11. Same as Fig. 5, but for the Kuroshio region. Kyushu Island and Ryukyu Island are denoted.

722

723 Fig. 12. Same as Fig. 6, but for the Kuroshio region in June. Contours indicate 0.1 (thin contour) and 0.2  
724 mm/hr (thick contour) of the amplitude shown in Fig. 10 (c).

725

726 Fig. 13. Same as Fig. 8, but for the Kuroshio region. Note that the color-scale values for panel (a) is wider  
727 than those for Fig. 8a.

728

729 Fig. 14. Same as Fig. 9, but for the Kuroshio region in June. The blue line indicates a box for the off-shore  
730 diurnal precipitation maximum ( $29^{\circ}$ – $30^{\circ}$ N,  $125^{\circ}$ – $126^{\circ}$ E), red line indicates a box for the near-shore diurnal  
731 precipitation maximum ( $28^{\circ}$ – $29^{\circ}$ N,  $128^{\circ}$ – $129^{\circ}$ W), and green line indicates a box to the east of the  
732 near-shore maximum ( $27^{\circ}$ – $28^{\circ}$ N,  $130^{\circ}$ – $131^{\circ}$ W), corresponding to the west-northwest, middle, and  
733 east-southeast regions of the diurnal precipitation amplitude maximum in Fig. 10c.

734

735 Fig. 15. Schematics of some essential features of the diurnal precipitation and high cloud cycles over the  
736 Gulf Stream (a) and the Kuroshio in the East China Sea (b). The Gulf Stream and the Kuroshio are  
737 indicated by the green arrows. Diurnally modulated precipitations and high clouds are shown by rain drops  
738 and cloud shapes, respectively. Oval in panel (b) indicates large-scale Baiu-Meiyu rain/cloud band. The  
739 wavy arrows indicate southeastward phase propagation of diurnal precipitations and clouds. In both regions,  
740 strong diurnally modulated precipitation and cloud cycles are found over the Gulf Stream and the Kuroshio,  
741 with southeastward phase propagation. Somewhat similar diurnal cycles are found to the east of the Gulf  
742 Stream with weaker amplitudes. The strong diurnal cycle over the Kuroshio is embedded in large-scale  
743 Baiu-Meiyu rainband, which does not have prominent diurnal cycles.

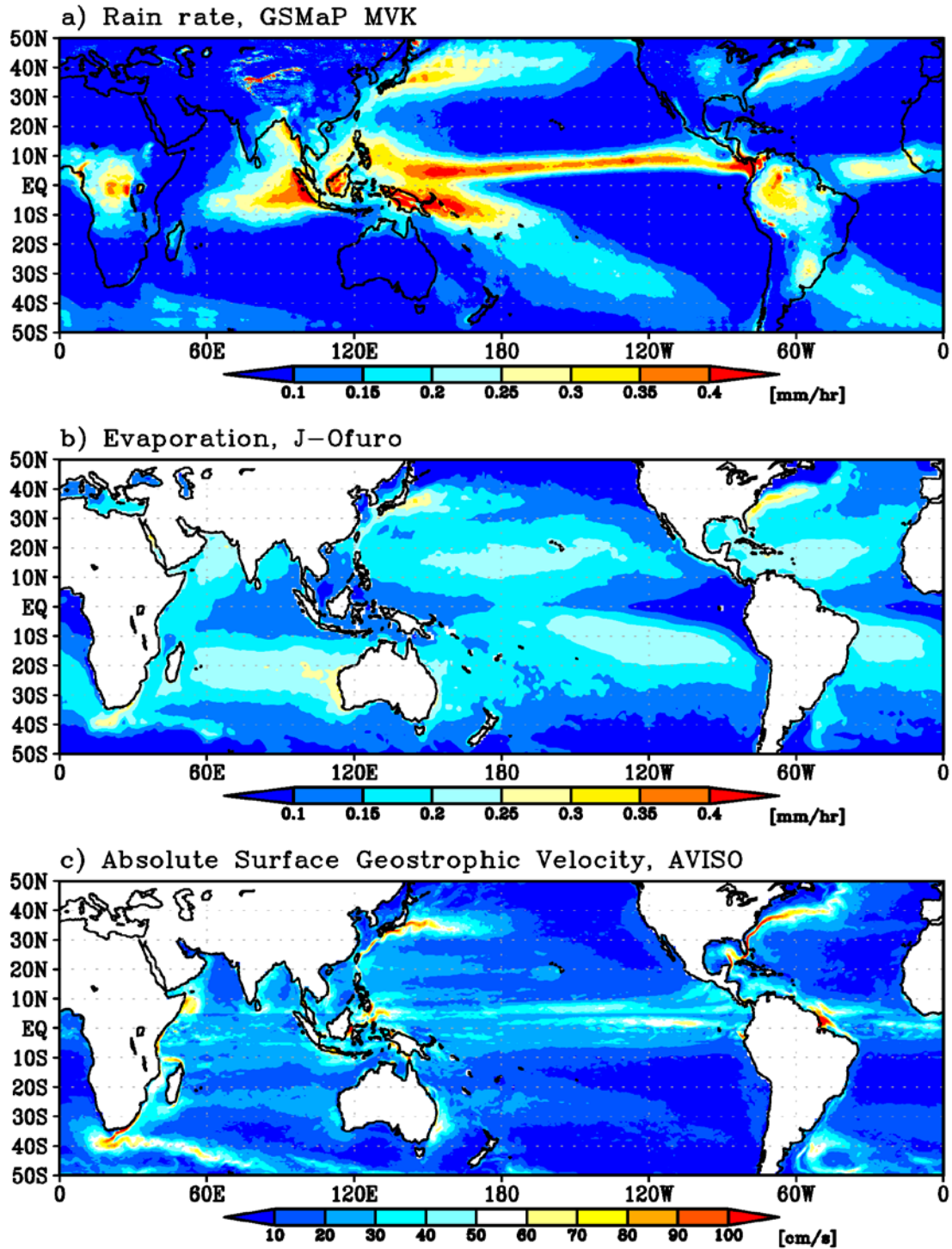


Fig. 1. Annual mean climatology of a) rain rate from GSMaP MVK from March 2000 to November 2010, b) evaporation from the J-Ofuro dataset from January 2000 to December 2006, c) surface geostrophic current velocities provided by AVISO from January 2000 to December 2010.

## Diurnal Precipitation, JJA (GSMaP-MVK)

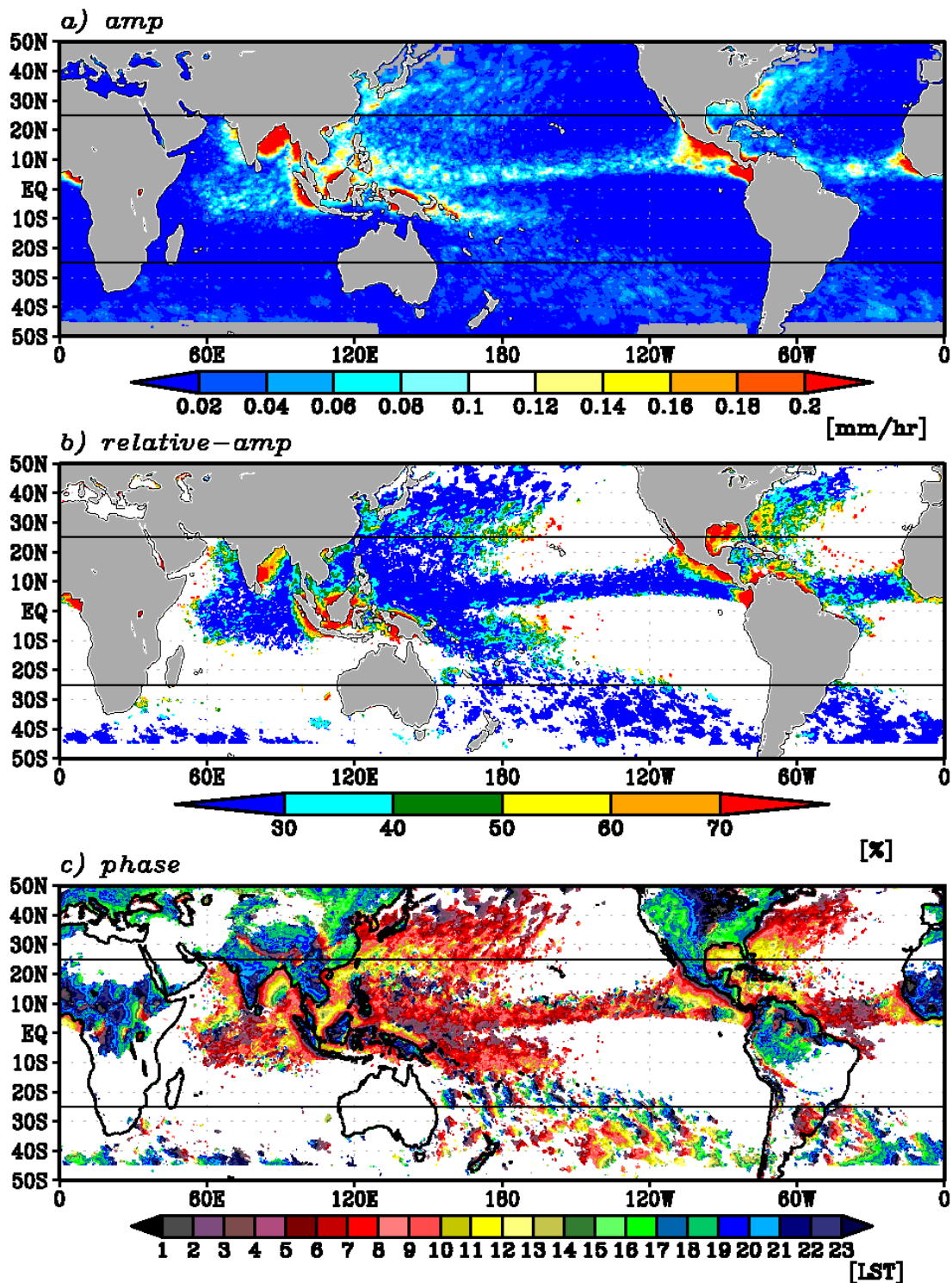


Fig. 2 a) Amplitude, b) relative amplitude and c) phase of diurnal precipitation cycle in boreal summer (June-August). Gray areas over the ocean in panel (a) are excluded from the analysis, because missing data rate due to presence of ice is larger than 20%. The values in panels (b, c) are drawn for the region where the amplitudes are larger than 0.02 mm/hr. Horizontal lines indicate 25°N/S.

### Diurnal Precipitation, DJF (GSMaP-MVK)

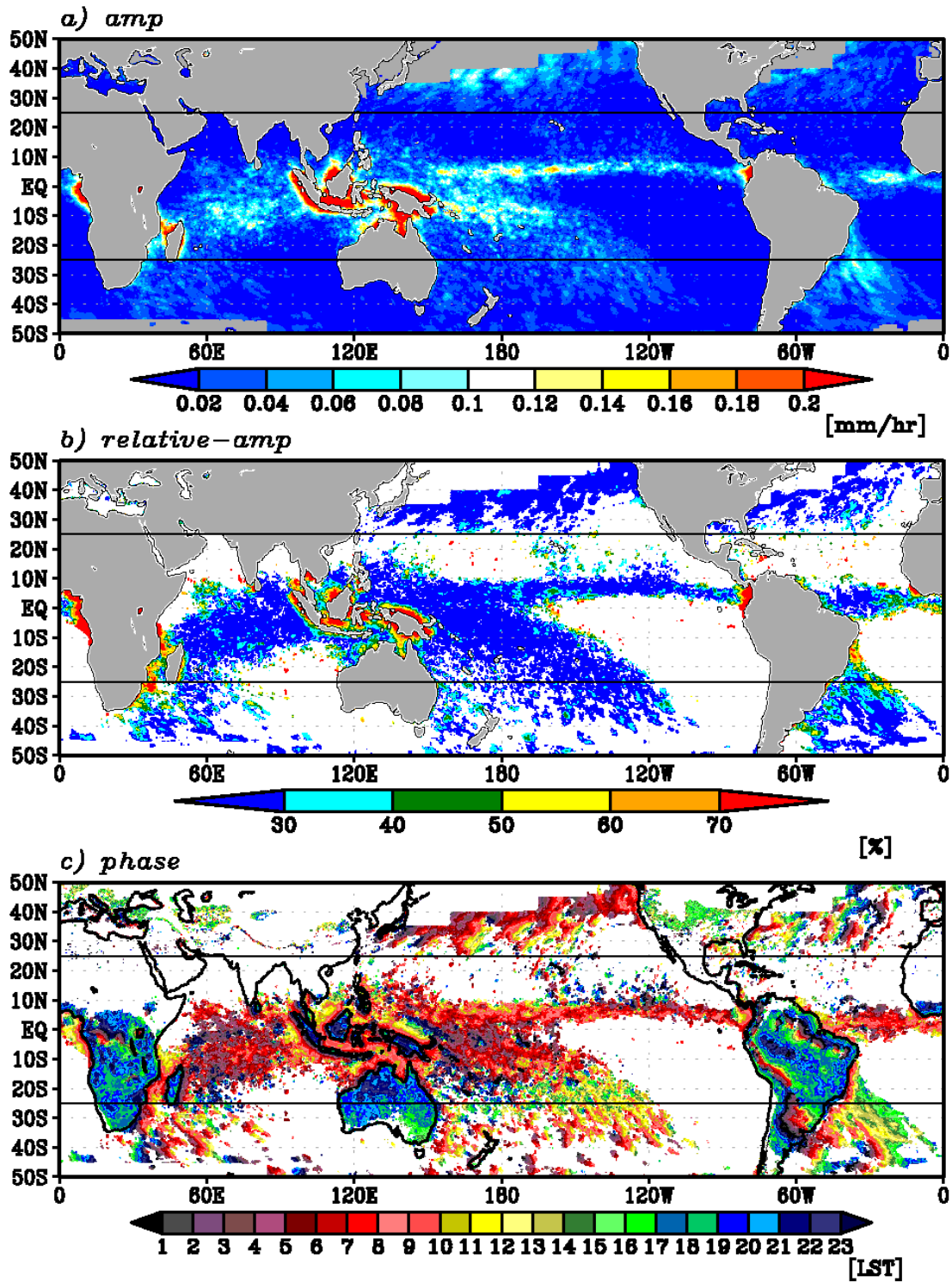


Fig. 3. Same as Fig. 2, but for the boreal winter (December–February).

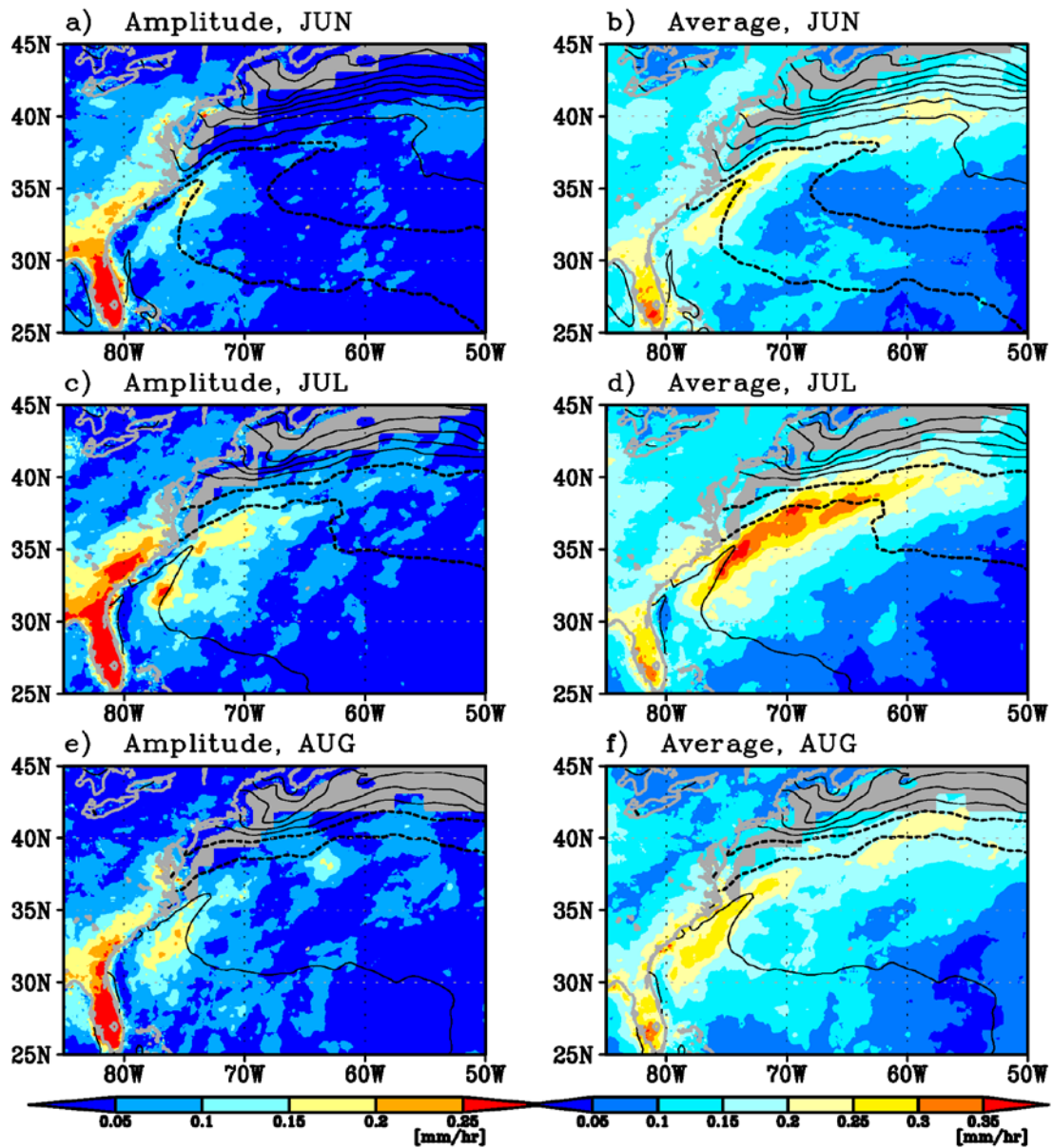


Fig. 4. Amplitudes of 24-hour diurnal cycle (left) and mean rain rate (right) of precipitations over the Gulf Stream region in June (top), July (middle) and August (bottom). Gray areas in left panels are excluded from the analysis, because missing data rate due to presence of ice is larger than 20%. Contours in each panel indicate SSTs with a contour interval of every 2°C and dashed contours for 24° and 26°C.

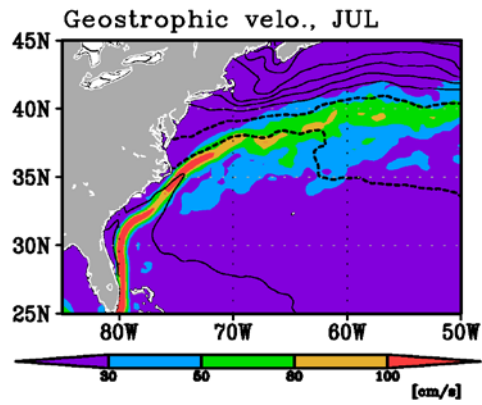


Fig. 5. Climatological absolute surface geostrophic velocity derived from satellite altimeter (color) and SSTs (contours) with a contour interval of every 2°C and dashed contours for 24° and 26°C in July.

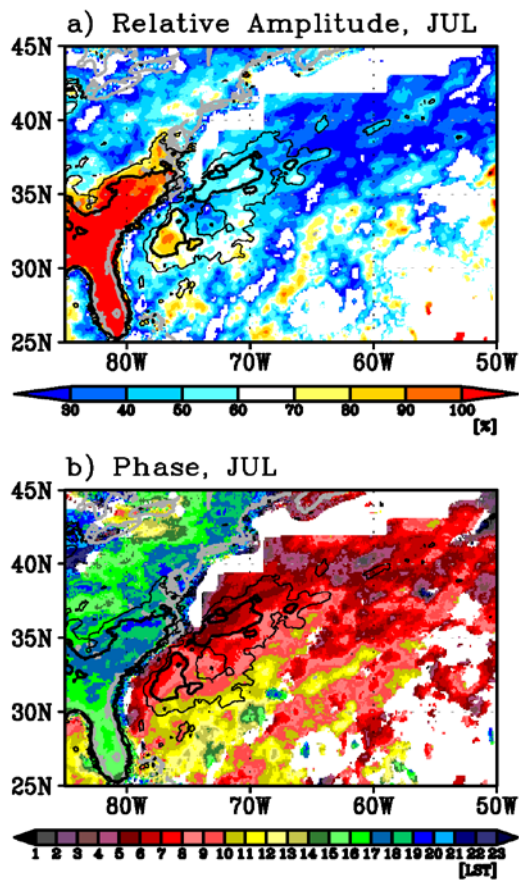


Fig. 6. a) Relative amplitudes and b) phases of the precipitation diurnal cycle over the Gulf Stream region in July. Phases shown by the time of maximum value of 24-hour cycle in LST. Contours indicate 0.1 (thin contour) and 0.15 mm/hr (thick contour) of the amplitudes shown in Fig. 4 (c). White regions are either missing data, due to presence of ice being larger than 20%, or the amplitudes shown in Fig. 4 (c) are smaller than 0.02 mm/hr.

*Correlation, along 32.05N*

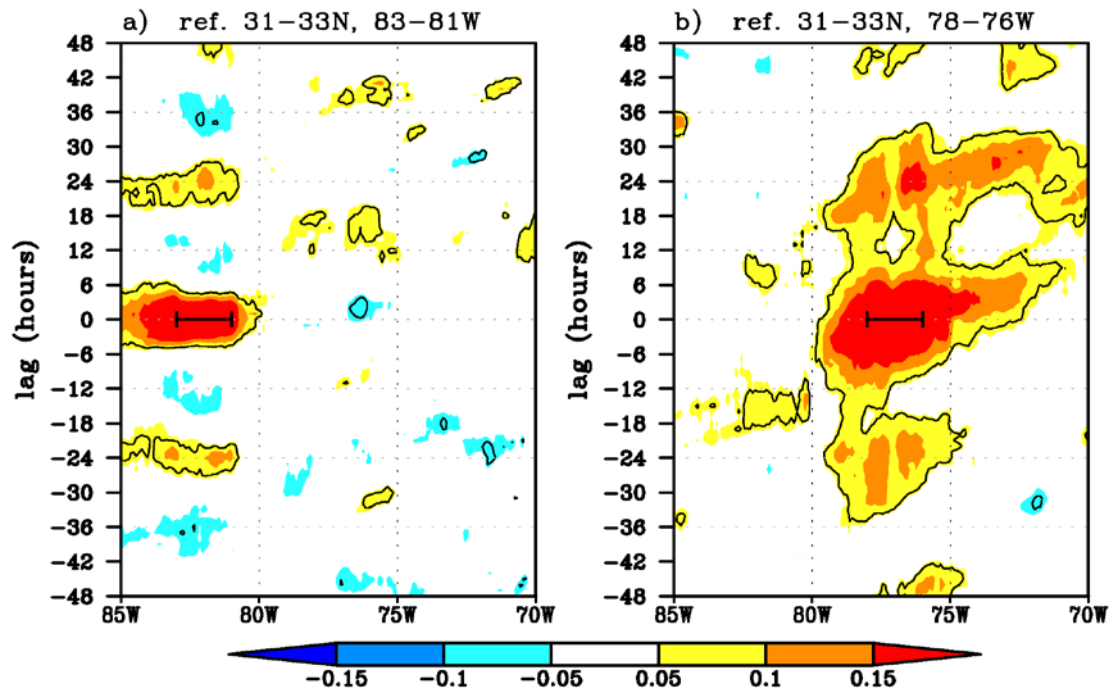


Fig. 7. Lag correlation coefficients at each grid point along 32.05N onto the reference area-averaged precipitation time series (a) in a region 83–81°W, 31–33°N over land and (b) in a region 78–76°W, 31–33°N over the ocean. Positive lags indicate reference time series leading to data at each grid point.

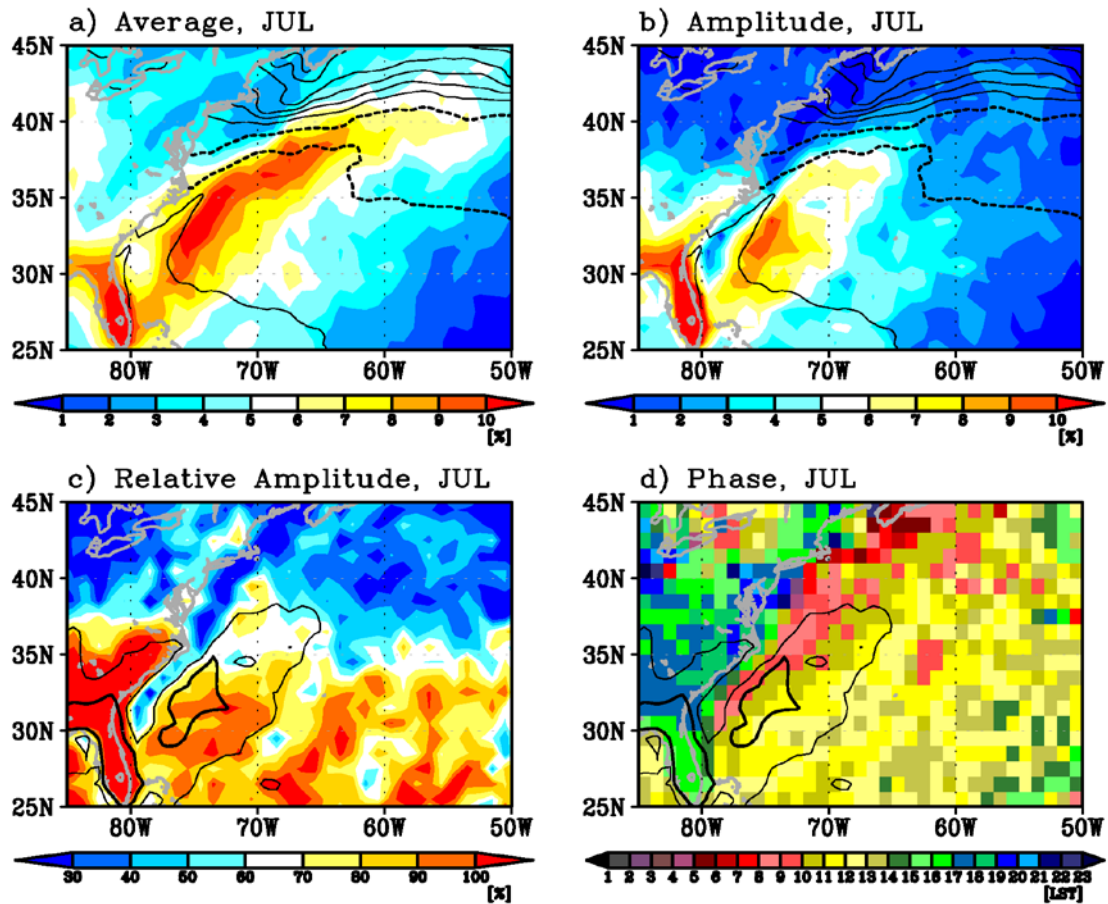
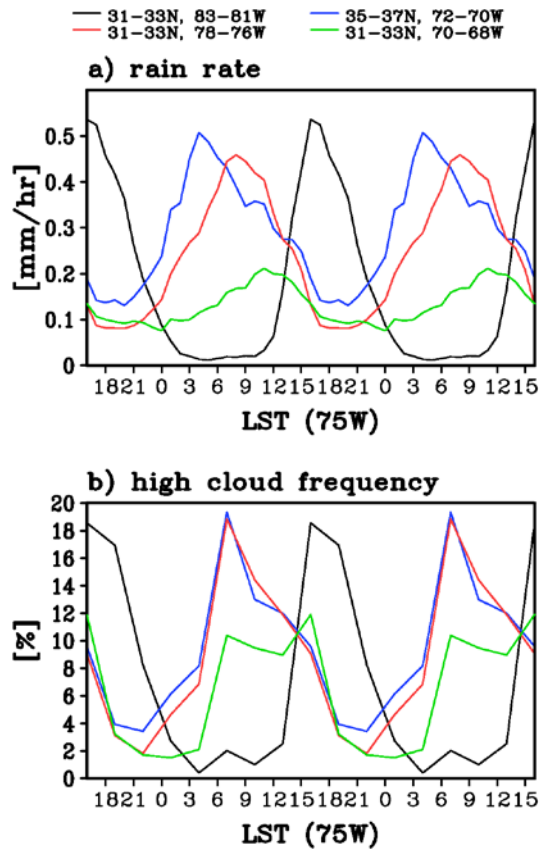


Fig. 8. a) average, b) amplitudes, c) relative amplitudes and d) phases of occurrence rate of high cloud estimated from OLR over the Gulf Stream region in July. Phases are shown by the time of maximal value of 24-hour cycle in LST. Contours in panels (a) and (b) are SSTs with a contour interval of  $2^{\circ}\text{C}$ , where dashed contours indicate  $24^{\circ}$  and  $26^{\circ}\text{C}$ , whereas contours in panels (b) and (c) are diurnal amplitudes of 5 and 8 %.



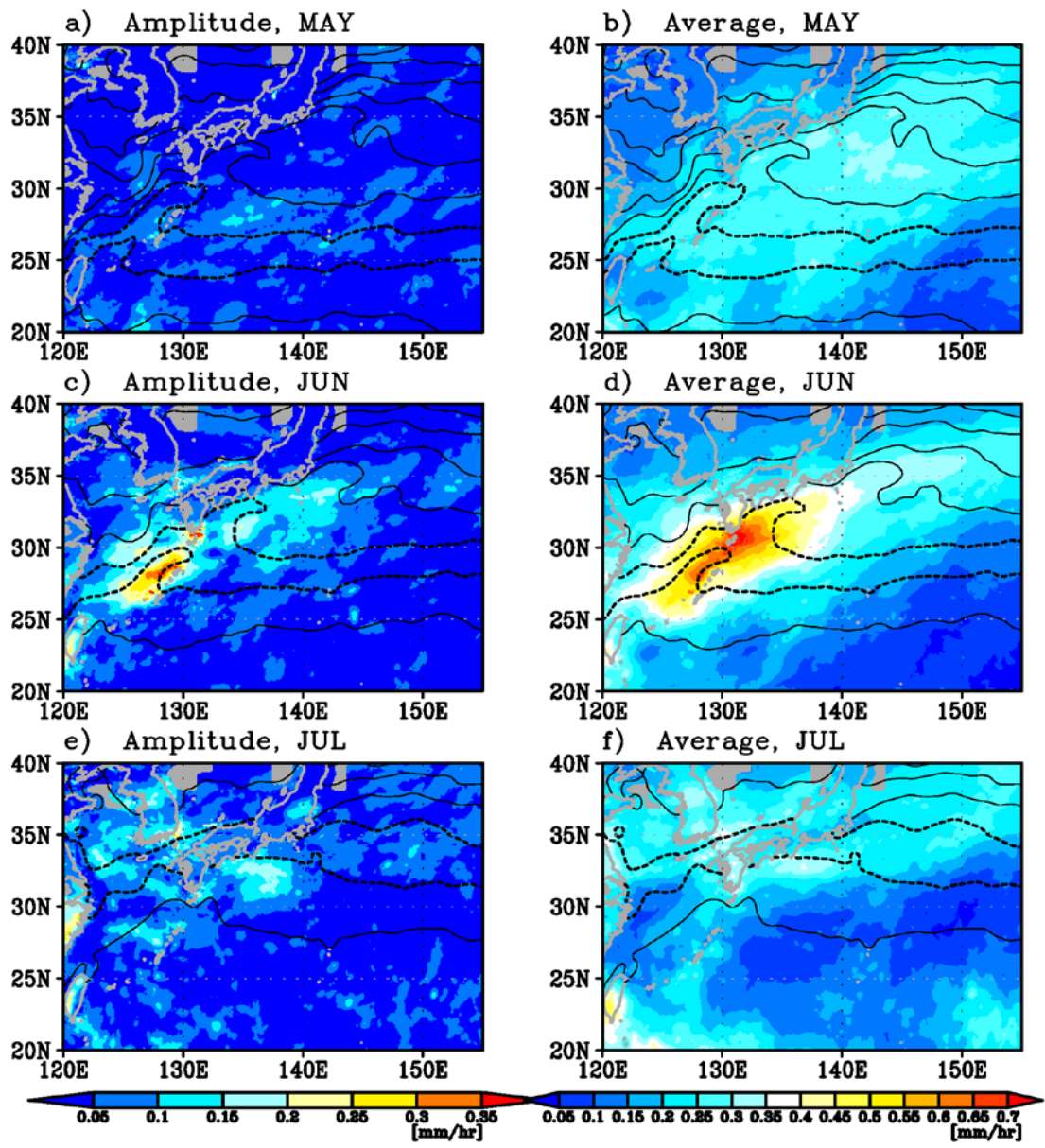


Fig. 10. Same as Fig. 4, but for the Kuroshio region in May (top), June (middle) and July (bottom). Note that the color-scale values are larger than those in Fig. 4.

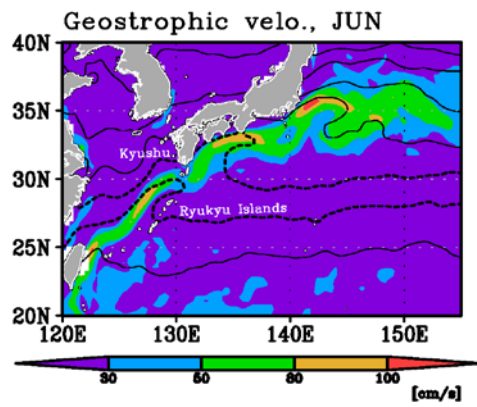


Fig. 11. Same as Fig. 5, but for the Kuroshio region. Kyushu Island and Ryukyu Island are denoted.

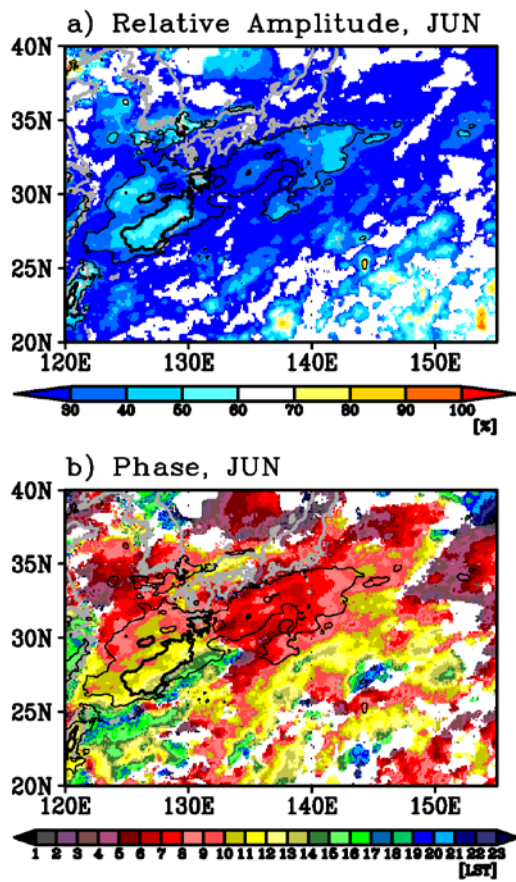


Fig. 12. Same as Fig. 6, but for the Kuroshio region in June. Contours indicate 0.1 (thin contour) and 0.2 mm/hr (thick contour) of the amplitude shown in Fig. 10 (c).

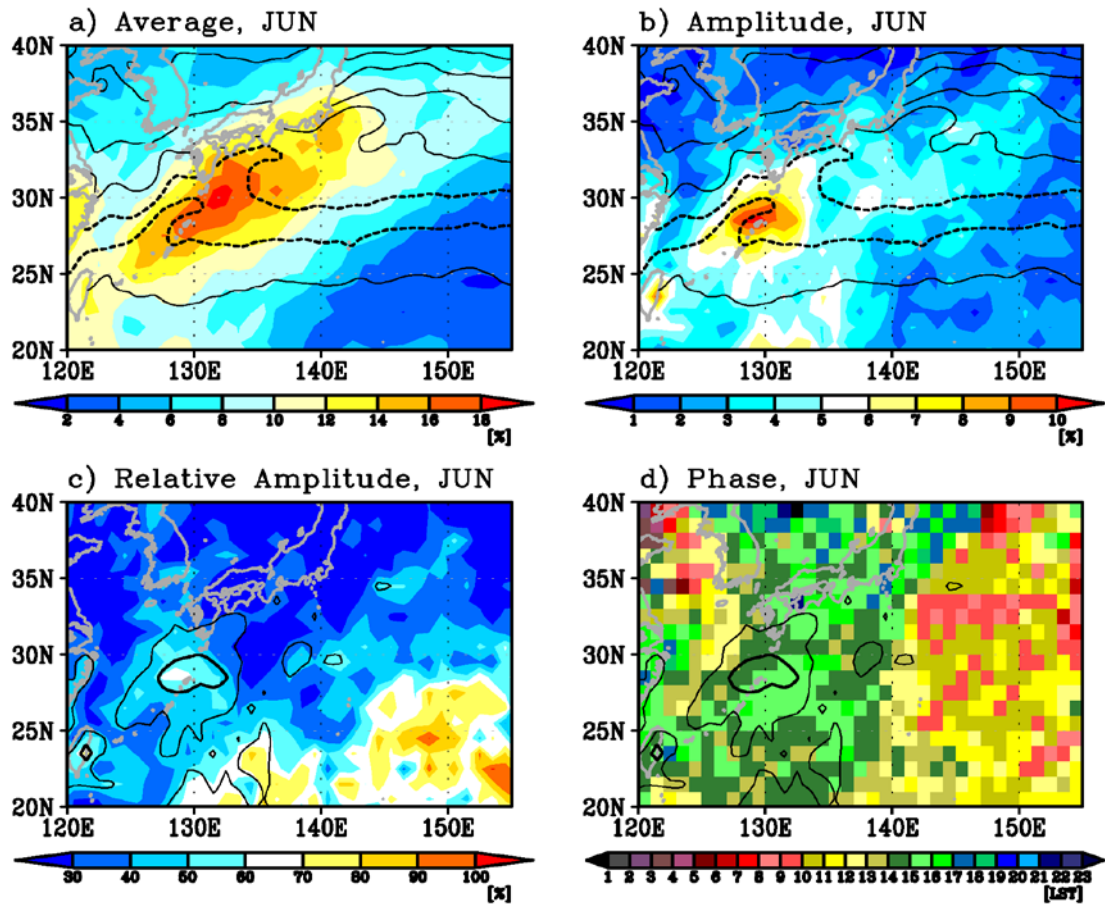


Fig. 13. Same as Fig. 8, but for the Kuroshio region. Note that the color-scale values for panel (a) is wider than those for Fig. 8a.

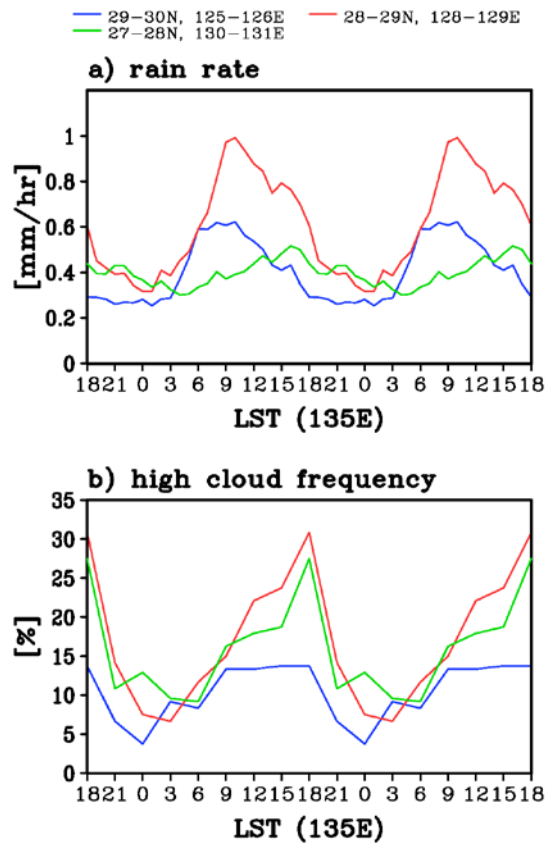


Fig. 14. Same as Fig. 9, but for the Kuroshio region in June. The blue line indicates a box for the off-shore diurnal precipitation maximum (29–30°N, 125–126°E), red line indicates a box for the near-shore diurnal precipitation maximum (28°–29°N, 128°–129°W), and green line indicates a box to the east of the near-shore maximum (27°–28°N, 130°–131°W), corresponding to the west-northwest, middle, and east-southeast regions of the diurnal precipitation amplitude maximum in Fig. 10c.

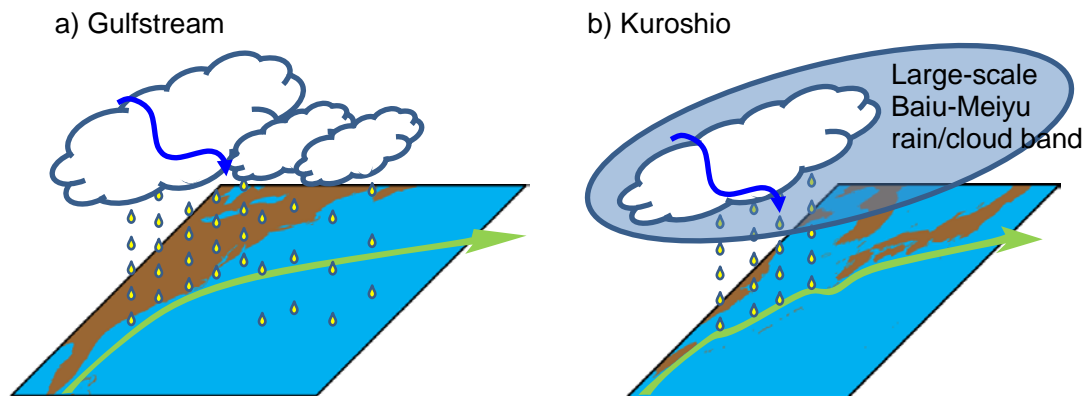


Fig. 15. Schematics of some essential features of the diurnal precipitation and high cloud cycles over the Gulf Stream (a) and the Kuroshio in the East China Sea (b). The Gulf Stream and the Kuroshio are indicated by the green arrows. Diurnally modulated precipitations and high clouds are shown by rain drops and cloud shapes, respectively. Oval in panel (b) indicates large-scale Baiu-Meiyu rain/cloud band. The wavy arrows indicate southeastward phase propagation of diurnal precipitations and clouds. In both regions, strong diurnally modulated precipitation and cloud cycles are found over the Gulf Stream and the Kuroshio, with southeastward phase propagation. Somewhat similar diurnal cycles are found to the east of the Gulf Stream with weaker amplitudes. The strong diurnal cycle over the Kuroshio is embedded in large-scale Baiu-Meiyu rainband, which does not have prominent diurnal cycles.